J. Fluid Mech. (2014), *vol.* 747, *pp.* 186–217.
doi:10.1017/jfm.2014.137

Turbulent flow over superhydrophobic surfaces with streamwise grooves

S. Türk[1], G. Daschiel[2], A. Stroh[2], Y. Hasegawa[3] and B. Frohnapfel[2,†]

[1]Graduate School of Computational Engineering, Technische Universität Darmstadt, Dolivostr. 15, 64293 Darmstadt, Germany

[2]Institute of Fluid Mechanics, Karlsruhe Institute of Technology, Kaiserstr. 10, 76131 Karlsruhe, Germany

[3]Institute of Industrial Science, The University of Tokyo, 4-6-1 Komaba, Meguro-ku, Tokyo 153-8505, Japan

(Received 23 August 2013; revised 14 January 2014; accepted 2 March 2014; first published online 14 April 2014)

We investigate the effects of superhydrophobic surfaces (SHS) carrying streamwise grooves on the flow dynamics and the resultant drag reduction in a fully developed turbulent channel flow. The SHS is modelled as a flat boundary with alternating no-slip and free-slip conditions, and a series of direct numerical simulations is performed with systematically changing the spanwise periodicity of the streamwise grooves. In all computations, a constant pressure gradient condition is employed, so that the drag reduction effect is manifested by an increase of the bulk mean velocity. To capture the flow properties that are induced by the non-homogeneous boundary conditions the instantaneous turbulent flow is decomposed into the spatial-mean, coherent and random components. It is observed that the alternating no-slip and free-slip boundary conditions lead to the generation of Prandtl's second kind of secondary flow characterized by coherent streamwise vortices. A mathematical relationship between the bulk mean velocity and different dynamical contributions, i.e. the effective slip length and additional turbulent losses over slip surfaces, reveals that the increase of the bulk mean velocity is mainly governed by the effective slip length. For a small spanwise periodicity of the streamwise grooves, the effective slip length in a turbulent flow agrees well with the analytical solution for laminar flows. Once the spanwise width of the free-slip area becomes larger than approximately 20 wall units, however, the effective slip length is significantly reduced from the laminar value due to the mixing caused by the underlying turbulence and secondary flow. Based on these results, we develop a simple model that allows estimating the gain due to a SHS in turbulent flows at practically high Reynolds numbers.

Key words: drag reduction, flow control, turbulent flows

1. Introduction

The potential reduction of skin friction drag in turbulent flows is of large economical and ecological interest and has continuously been investigated over

† Email address for correspondence: frohnapfel@kit.edu

the past few decades. A variety of different drag-reducing techniques are known today which are commonly classified in passive, active and reactive flow control mechanisms (Gad-El-Hak 2007). From an application point of view passive flow control techniques are most appealing since they do neither require the installation of additional actuators and sensors nor the continuous energy input to run the control (Spalart & McLean 2011). The use of superhydrophobic surfaces (SHS) for passive control of skin friction drag has been investigated in both flow regimes, laminar and turbulent, and it was demonstrated that SHS have promising potential for application in turbulent flows (Rothstein 2010).

A SHS usually consists of a thin-film hydrophobic coating with a certain roughness pattern. Gas bubbles are trapped in the cavities of the roughness pattern, locally providing a gas–liquid interface with almost zero shear instead of the usual no-slip interface along a solid wall. The superhydrophobicity of a surface is only obtained if the fluid does not wet the cavities, e.g. remains in the Cassie state (Cassie & Baxter 1944; Rothstein 2010).

Philip (1972) models the SHS as an alternating boundary condition between no-slip and free-slip using the Navier boundary condition, originally proposed by Navier (1823), for solid–fluid interfaces on microscopic scale. By averaging over the entire surface, an average slip velocity at the wall, u_s, is obtained:

$$u_s = l_s \left(\frac{\partial u}{\partial y} \right)_w \tag{1.1}$$

where l_s denotes the effective slip length relating the slip velocity and the velocity gradient at the wall (subscript w). For Stokes flow through a two-dimensional channel with a superhydrophobic roughness pattern consisting of longitudinal or transversal grooves, Philip (1972) analytically shows that the effective slip length over streamwise grooves is exactly twice as large as that over transverse ones. The corresponding solution for a flow in a circular tube is given in Lauga & Stone (2003). It can be shown that for flows over longitudinal grooves, the solution derived by Philip (1972) holds for a fully developed laminar regime regardless of the Reynolds number, since the streamwise uniformity ensures that all nonlinear terms do not influence the resulting flow field. In the case of transversal grooves, however, the nonlinear terms cannot be neglected and thus the effective slip length exhibits a Reynolds number dependency in the laminar regime. Consequently, the effective slip length over transversal grooves reduces with increasing Reynolds number, and thus deviates from that at the Stokes limit (Woolford, Maynes & Webb 2008). A unified expression for the effective slip length for different geometries and Reynolds numbers in the laminar regime is provided by Woolford *et al.* (2008), where the influence of the cavity depth on the overall drag reduction and the assumption of a flat gas–liquid interface are also discussed. It is shown that the assumption of a flat interface, which we take in the present work, is valid if the width of the cavity is roughly equal to its depth.

In addition to the mentioned analytical and numerical studies, experiments on drag reduction resulting from SHS in laminar flow have also been conducted by, for example, Ou, Perot & Rothstein (2004) or Maynes *et al.* (2007). In these experiments the pressure drop is monitored as a function of varying flow rates and the results are in agreement with the analytical derivations by Philip (1972): drag reduction in laminar flow is increased with decreasing solid fraction and increasing cavity width; longitudinal grooves generally have higher drag reduction potential than transversal grooves.

Considering that most engineering flows are turbulent such that the friction drag is significantly increased compared with laminar flows, the potential application of a SHS to turbulent flow for drag-reducing purposes is of great interest. First experiments by Daniello, Waterhouse & Rothstein (2009) have demonstrated that SHS turn out to be quite promising in the turbulent regime. They found significant drag reduction with a slip length much smaller than the channel height. In laminar flows, in contrast, the effective slip length has to be of the same order as the channel height to achieve a significant drag reduction rate. This difference is caused by the strong velocity gradients at the wall characteristic for turbulent flows: following (1.1) a larger velocity gradient results in a larger slip velocity for a given slip length.

The effect of SHS on turbulent flows has also been investigated numerically. Min & Kim (2004) model the SHS with a uniform slip length over a flat fluid–solid boundary. They show that streamwise slip causes drag reduction if a constant flow rate (CFR) is prescribed, while spanwise slip enhances turbulence near the wall, and thus contributes to drag increase. Based on these results, Fukagata, Kasagi & Koumoutsakos (2006) develop a theoretical model of the friction drag reduction over a SHS with arbitrary streamwise and spanwise slip lengths. This model shows that significant drag reduction can be achieved, even at high Reynolds numbers, with a slip length of the order of ten wall units. This result is confirmed by Busse & Sandham (2012) who perform an intensive parametric study for various combinations of streamwise and spanwise slip lengths. As part of the parameter study they report the inherent problem of turbulent drag reduction investigations at low Reynolds numbers and CFR: the flow laminarizes for high drag-reduction values that are realized with large streamwise slip lengths.

Martell, Perot & Rothstein (2009) first conducted direct numerical simulations (DNS) of turbulent channel flow for which the SHS is modelled by alternating local free-slip and no-slip wall boundary conditions without employing the effective slip length model. In such a simulation, the effective slip length depends on the groove geometry and is obtained as a result of the computation. In consecutive work Martell, Rothstein & Perot (2010) consider several layouts of streamwise and spanwise oriented grooves as well as surface structures consisting of posts in the Reynolds number range of $Re_\tau = 180$–590. In these simulations, which are partly complemented by experiments (Daniello *et al.* 2009), only one of the two channel walls has a superhydrophobic property such that the flow is not symmetric around the channel centreline and different shear stresses occur at the two walls. The simulations are run under a constant pressure gradient (CPG), i.e. a fixed Re_τ. Drag reduction is evaluated based on the difference in wall shear stress on the SHS wall and on a wall in a no-slip reference channel at the same Re_τ. The reduction of the wall shear stress is found to be highest for posts and streamwise-oriented grooves. In addition, the tendency towards increasing drag reduction for an increase of the feature spacing is observed.

Within the present study we aim to systematically investigate the impact of the structural spacing of a SHS pattern with streamwise grooves on the fully developed turbulent flow state. This pattern has the highest potential for drag reduction if the solid fraction, Φ, of the surface is fixed (Martell *et al.* 2010). In contrast to previous studies we perform DNS of turbulent channel flow including superhydrophobic boundary conditions on both channel walls under CPG conditions. This set-up, for which the wall shear stress and thus Re_τ is kept constant on both channel walls, ensures the absence of relaminarization effects and the gain of SHS is given by an increase in flow rate (which also leads to a reduction of the non-dimensional

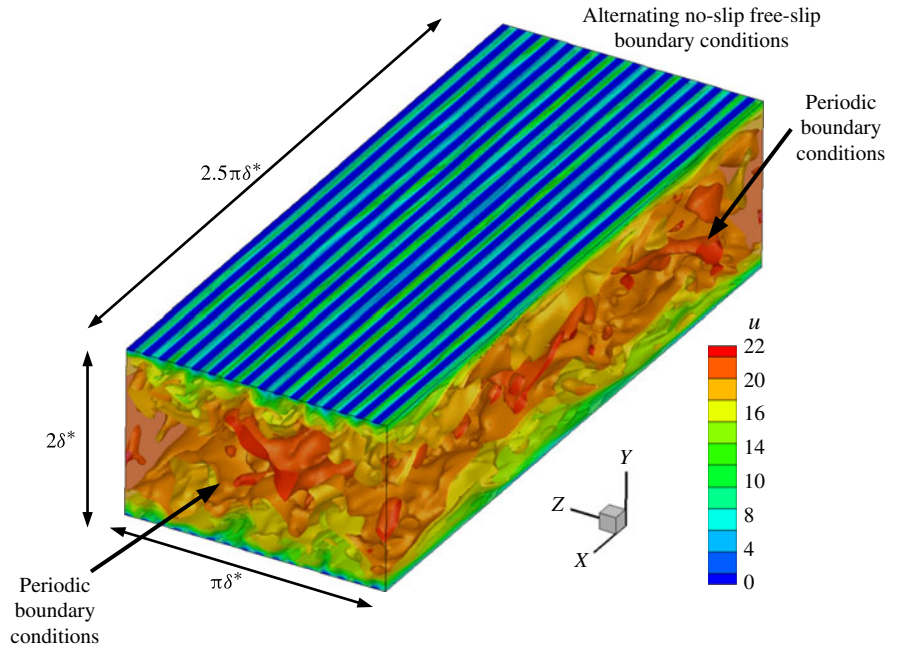

FIGURE 1. Illustration of the computational domain and the instantaneous velocity field.

c_f value). Most importantly, this particular flow condition allows us to derive a simple mathematical relationship between the achieved gain in flow rate and the two corresponding dynamical contributions, i.e. the effective slip length and the losses due to enhanced turbulent motion over SHS.

By systematically changing the width of the streamwise grooves, we analyse the quantitative contributions of each component to the resultant flow rate and thus provide a link to the existing analytical solution for laminar flow conditions (Philip 1972). Based on these results, a simple modelling strategy that allows estimating the gain achieved by SHS in turbulent flows is presented.

2. Numerical conditions and methods

2.1. *Governing equations and numerical method*

In the present work DNS are performed for a fully developed turbulent channel flow driven by a CPG. The applied boundary conditions and the computational domain are illustrated in figure 1, where $x = x_1$, $y = x_2$ and $z = x_3$ correspond to the streamwise, wall-normal and spanwise direction, respectively. The flow is bounded by alternating no-slip free-slip boundary conditions on the bottom ($y = 0$) and top wall ($y = 2\delta$), while periodic boundary conditions are applied in streamwise and spanwise direction.

For an incompressible Newtonian fluid, the flow has to satisfy the continuity and momentum equations in the following form:

$$\frac{\partial u_i^*}{\partial x_i^*} = 0 \tag{2.1}$$

$$\rho^* \frac{\mathrm{D}u_i^*}{\mathrm{D}t^*} = -\frac{\partial p^*}{\partial x_i^*} + \mu^* \frac{\partial^2 u_i^*}{\partial x_j^{*2}} \tag{2.2}$$

Re_τ	Grid size	Domain size	Δx	Δy_{min}	Δz
180	$128 \times 129 \times 128$	$2.5\pi\delta \times 2\delta \times \pi\delta$	11.0	0.1	4.4
180	**$128 \times 129 \times 256$**	**$2.5\pi\delta \times 2\delta \times \pi\delta$**	**11.0**	**0.1**	**2.2**
180	$256 \times 129 \times 256$	$5\pi\delta \times 2\delta \times \pi\delta$	11.0	0.1	2.2
180	$256 \times 129 \times 256$	$2.5\pi\delta \times 2\delta \times \pi\delta$	5.5	0.1	2.2
180	$512 \times 129 \times 256$	$2.5\pi\delta \times 2\delta \times \pi\delta$	2.75	0.1	2.2
180	$128 \times 129 \times 512$	$2.5\pi\delta \times 2\delta \times \pi\delta$	11.0	0.1	1.1
180	$128 \times 129 \times 1024$	$2.5\pi\delta \times 2\delta \times \pi\delta$	11.0	0.1	0.55
180	$128 \times 129 \times 512$	$2.5\pi\delta \times 2\delta \times 2\pi\delta$	11.0	0.1	2.2
180	$128 \times 129 \times 1024$	$2.5\pi\delta \times 2\delta \times 4\pi\delta$	11.0	0.1	2.2

TABLE 1. Domain properties of the present DNS. The bold line highlights the configuration of the standard case.

where p^* is the static pressure and μ^* is the dynamic viscosity. Throughout this paper, the asterisk denotes a dimensional quantity. Otherwise quantities are non-dimensionalized by the friction velocity, u_τ^*, and the kinematic viscosity, ν^*, such that $u = u^*/u_\tau^*$, $x_i = x_i^* u_\tau^*/\nu^*$ and $t = t^* u_\tau^{*2}/\nu^*$ (wall units). Note that, as the pressure gradient is kept constant during the simulation, u_τ^* is constant consequently. The same holds for the friction Reynolds number given by

$$Re_\tau = \frac{u_\tau^* \delta^*}{\nu^*}, \tag{2.3}$$

where δ^* is the half-channel height. By doing so, the gain due to a SHS is measured in terms of an increase in flow rate compared to a turbulent channel flow with purely no-slip walls at top and bottom. This approach is chosen since the alternative set-up in which a CFR is prescribed, will lead to very low friction Reynolds numbers for the large drag reduction that is expected with SHS. Potential changes in the turbulence properties due to the presence of SHS might be masked through this Reynolds number effect.

As numerical scheme, a fractional step method on a staggered grid is applied. For spatial discretization a second-order finite difference method is used while for temporal discretization, the solver employs the second-order Adams–Bashforth method for the convection terms and the Crank–Nicolson method for the viscous terms. The grid resolution and the grid spacing are given in table 1. In particular, the resolution in spanwise direction is critical in the present set-up and is discussed further in the following section. To limit the overall computational costs we choose a rather coarse grid in streamwise direction, i.e. $\Delta x = 11$, and a relatively short computational domain. By doubling and quadruplicating the number of grid points in streamwise direction for selected cases it was confirmed that the main results presented in this paper, i.e. effective slip length and the profile of the Reynolds shear stress throughout the channel (i.e. turbulent losses), are hardly affected by the streamwise grid spacing. The difference in the resultant bulk mean velocity remains less than 2 %. Concerning the streamwise extend of the computational box selected cases were rerun with twice the streamwise box size. It is confirmed that the results presented in this paper are hardly affected by this variation. Specifically, the corresponding difference of U_b is less than 1 %. However, we note that, even for a streamwise extend of $5\pi\delta$, the two-point correlation of the random streamwise velocity fluctuations in the near-wall

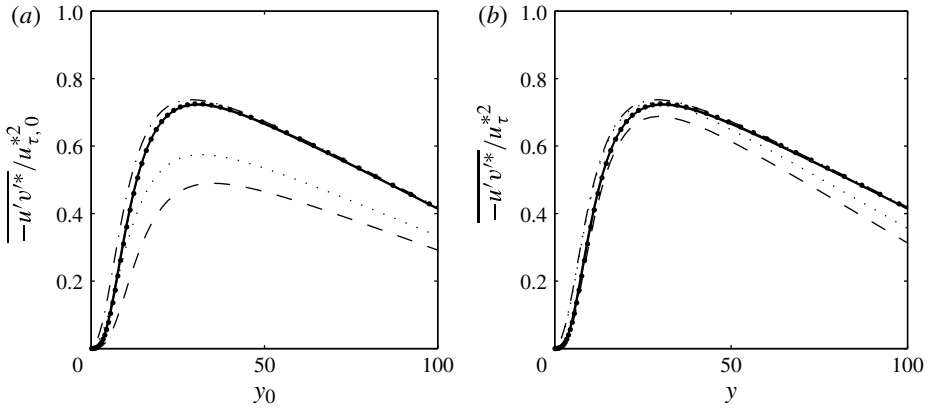

FIGURE 2. Reynolds shear stress $-\overline{u'v'}$ (*a*) normalized by the wall shear velocity $u^*_{\tau,0}$ of the reference case (no-slip) (*b*) normalized by the actual u^*_τ. Curves: ——, no-slip reference channel; – –, CFR streamwise slip; · · · , CFR streamwise and spanwise slip; ●, CPG streamwise slip; – · –, CPG streamwise and spanwise slip.

region ($y^+ < 10$) does not fully decrease to zero if the spanwise location in the centre of the free-slip region is considered. In general, the spanwise average of the streamwise two-point correlations shows only very small differences compared with the results of a regular no-slip channel.

All statistics presented in the following are obtained for an integration time of $t = 10\,440$ with a time step of $\Delta t = 0.036$. The present code has been validated for the fully developed turbulent flow over no-slip walls with standard literature data (Kim, Moin & Moser 1987).

2.2. *Superhydrophobic boundary condition*

Since there is no data available in the literature for superhydrophobic boundary conditions under CPG we first verify our implementation of streamwise and spanwise slip conditions by reproducing the data of Min & Kim (2004) for a homogeneous slip length of $l_s = 3.566$ under CFR conditions. The case of streamwise slip only (Case 1 in Min & Kim (2004)) as well as that for combined streamwise and spanwise slip (Case 3 in Min & Kim (2004)) is considered for verification purposes. The obtained slip velocity for streamwise slip deviates less than 1 % from the corresponding literature result (of $u_s = 3.006$). The test case of combined streamwise and spanwise slip is also reproduced with less than 1 % deviation from the literature result (of $u_s = 3.238$). To illustrate the difference between CFR and CPG conditions for SHS, the same simulations are run for CPG conditions. In this case the resulting slip velocities have to coincide with the value of the prescribed streamwise slip lengths since $\partial u/\partial y = 1$ holds for CPG conditions. Since drag is not changed by definition, the CPG condition yields an increase of the flow rate: 23 % for Case 1 and 13 % for Case 3. Differences between CFR and CPG are naturally also visible in the Reynolds stresses.

Figure 2 exemplary shows the distribution of the Reynolds shear stress, $-\overline{u'v'}$, for both cases (i.e. CFR and CPG) when either only streamwise or a combination of streamwise and spanwise slip is applied. The Reynolds shear stress is chosen since it is strongly linked to the friction factor, c_f (Fukagata, Iwamoto & Kasagi

2002), and is thus an essential quantity when skin friction drag reduction is to be discussed. In figure 2(*a*), $-\overline{u'v'}$ obtained under CFR and CPG is presented in a normalization that is based on $u^*_{\tau,0}$, i.e. the wall shear velocity of the reference case. In this case, $-\overline{u'v'}$ appears to be significantly damped in CFR. However, one cannot immediately conclude that SHS suppresses near-wall turbulence, because the wall friction is also reduced in CFR. The normalization of $-\overline{u'v'}$ based on the actual u^*_τ is shown in figure 2(*b*): the difference between CFR and the reference flow are less prominent. The slight remaining difference can be mainly attributed to the Reynolds number effect, since it is well known that the turbulent statistics are affected by the friction Reynolds number even in uncontrolled flow at the low Reynolds numbers considered here. For CPG (and also the reference flow) there is no difference between figure 2(*a*) and (*b*), since the reference and actual u^*_τ are identical by definition. In the case of CPG with streamwise slip only, the distribution of $-\overline{u'v'}$ is identical to that of the reference flow with no-slip walls. This suggests that the turbulent flow over a SHS is dynamically equivalent to that in a channel flow with no-slip walls moving at u_s. For combined streamwise and spanwise slip $-\overline{u'v'}$ slightly increases under CPG which is consistent with the conclusion of Min & Kim (2004) who show that spanwise slip leads to an increased turbulence activity in the near-wall region.

As seen from the above considerations, the interpretation of results can depend on the employed numerical conditions and the normalization of flow quantities. This issue is not specific to the current study, but common in flow control problems as discussed by Frohnapfel, Hasegawa & Quadrio (2012). Since the purpose of the present study is to investigate the essential effects of a SHS on the dynamics of wall turbulence under fully turbulent conditions, prescribing a constant wall friction is the most appropriate strategy. Therefore, we employ the CPG condition throughout this work.

In contrast to studies with a prescribed spatially uniform slip length we investigate SHS consisting of streamwise-oriented grooves in the following. In this set-up a homogeneous slip length is not given *a priori*, but the surface is modelled by alternating no-slip free-slip (i.e. no-shear) boundary conditions. These are applied at top and bottom wall of the channel in such a way that the problem is symmetric about the centre plane of the channel, and the effective slip length is obtained by considering the time- and space-averaged (in streamwise and spanwise direction) velocity field that results from the DNS. The implementation of this non-uniform boundary condition is verified by reproducing the laminar analytical solution of Philip (1972). The reproduction of the laminar solution shows that high spatial resolution is required in order to handle the discontinuity that is introduced between slip and no-slip areas. Systematic grid refinement under laminar flow conditions reveals that this singularity in the boundary condition alters the convergence rate of the numerical scheme: it is found to be of first order for the present case.

The SHS is characterized by the periodicity L as shown in figure 3 and the solid fraction Φ which is defined as $\Phi = d/L$. The investigated scenarios are summarized in table 2. A wide range of L values is investigated, ranging from 2 to 150 % of the channel height. To ensure that results for large L values are not influenced by the spanwise extend of the computational box the domain size was extended for these cases (see table 1). We note that it is questionable whether SHS that correspond to the largest L values can be realized under turbulent flow conditions in practice (see appendix A). However, it is still beneficial to consider such idealized situations in order to investigate the effects of L on near-wall turbulent dynamics alone from a fundamental viewpoint and also evaluate a maximum achievable gain in flow rate with SHS.

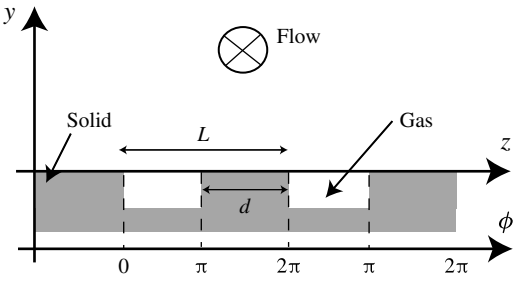

FIGURE 3. Schematic of a SHS with streamwise grooves and the corresponding phase ϕ.

Geometric wavelength, L	8.8	17.6	35.2	70.4	140.8	140.8	140.8	281.6	563.2
Spanwise resolution, Δz	0.55	0.55	1.1	2.2	2.2	0.55	2.2	2.2	2.2
Number of grid points per L, n	16	32	32	32	64	256	64	128	256
Normalized wavelength, $L/2\delta$	0.024	0.049	0.098	0.20	0.39	0.39	0.39	0.78	1.56
Solid fraction, Φ	0.5	0.5	0.5	0.5	0.25	0.5	0.75	0.5	0.5

TABLE 2. Considered configurations.

As mentioned above, the spanwise resolution (i.e. the resolution of the periodically varying boundary condition) is a critical issue for the numerical realization of the alternating boundary conditions of no-slip and free-slip. Therefore, a parametric study with varying resolution in the spanwise direction is carried out for three selected wavelengths of $L = 8.8$, 17.6 and 140.8 under turbulent flow conditions. The corresponding results are summarized in figure 4(*a*) where the resulting relative slip length, l_s/L, is plotted versus the spanwise resolution Δz. There is a clear grid dependency for small values of L which indicates that even higher resolution in spanwise direction (probably in combination with increased wall-normal and streamwise resolution) would be required to correctly capture l_s for small L. The trend in the present results indicates that the convergence rate of first order observed for laminar flow seems to also exist under turbulent conditions. If we assume that a linear extrapolation of the shown trend towards $\Delta z = 0$ yields a lower limit for the respective l_s, it is possible to estimate a relative error as a function of the grid points, n, employed per wavelength, L. Figure 4(*b*) indicates that n generally characterizes the achievable accuracy of our set-up. It can be concluded that $2^5 = 32$ grid points should be present over one wavelength L in order to reduce the relative error in l_s to less than 10 %. This requirement for the grid resolution becomes particularly tough for DNS with small L. However, the effect of SHS diminishes as L decreases and the resultant effective slip length at small $L < 35$ can be well predicted by the laminar analytical solution as will be shown in the following. In the range of comparatively large L where the difference between SHS in laminar and turbulent regimes is more prominent, sufficiently fine spanwise resolution can be achieved. Based on the observed dependencies shown in figure 4 the spanwise resolution is set as summarized in table 2.

2.3. *Decomposition of the velocity field*

Owing to the periodically varying boundary condition in the spanwise direction, it is likely that the statistical features of the turbulent velocity field show a similar

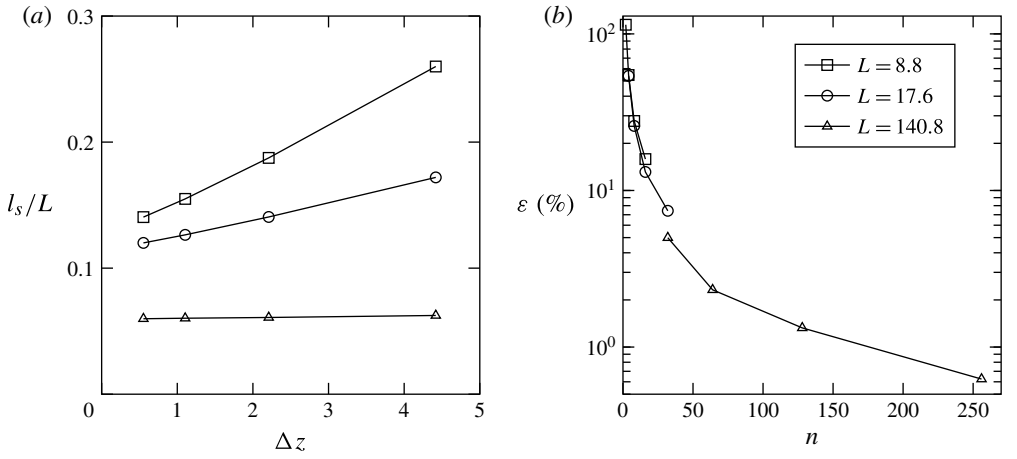

FIGURE 4. (*a*) Dependency of the relative slip length, l_s/L, on the spanwise resolution, Δz for different wavelength, L. (*b*) Upper bound estimation of the relative error in the determination of l_s as a function of the number of grid points, n, employed per wavelength, L.

periodicity. Accordingly, a phase-averaging operator leading to a triple decomposition as suggested by Reynolds & Hussain (1972) is introduced as

$$\langle f\rangle\,(\phi, y) = \frac{1}{N}\sum_{n=1}^{N}\int_t\int_x f\left(x, y, L\left(\frac{\phi}{2\pi}+n\right), t\right)\,\mathrm{d}x\,\mathrm{d}t, \tag{2.4}$$

where f is an arbitrary variable and a function of space and time, while ϕ is a phase with respect to the periodic structure as shown in figure 3 and N is the number of periods in the computational domain. Averaging $\langle f\rangle$ over ϕ results in the spatial mean

$$\bar{f}(y) = \frac{1}{2\pi}\int_0^{2\pi}\langle f\rangle\,(\phi, y)\,\mathrm{d}\phi. \tag{2.5}$$

Accordingly, coherent fluctuations are defined as

$$\tilde{f}(\phi, y) = \langle f\rangle\,(\phi, y) - \bar{f}(y). \tag{2.6}$$

Thus, any flow quantity can be decomposed as follows:

$$\begin{aligned} f(x, y, z, t) &= \langle f\rangle\,(\phi, y) + f''(x, y, z, t)\\ &= \bar{f}(y) + \tilde{f}(\phi, y) + f''(x, y, z, t), \end{aligned} \tag{2.7}$$

where a quantity with a double prime represent the deviation from the phase average and is referred to as random fluctuation throughout this paper. We also define the overall fluctuation as the deviation from the spatial mean

$$\begin{aligned} f'(x, y, z, t) &= f(x, y, z, t) - \bar{f}(y)\\ &= \tilde{f}(y, \phi) + f''(x, y, z, t). \end{aligned} \tag{2.8}$$

This is equivalent to the definition of a fluctuating component in the conventional Reynolds averaging for no-slip walls with a homogeneous spanwise direction. In the case of the hydrophobic surface with streamwise grooves, the overall fluctuations are given by a sum of coherent and random fluctuations as shown in (2.8). Accordingly, the correlation of two arbitrary quantities f and g can be obtained as

$$\overline{f'g'} = \overline{\tilde{f}\tilde{g} + f''g''}. \tag{2.9}$$

3. Impact of SHS on the turbulent flow field

3.1. *Effective slip length*

For laminar flow conditions the analytical solution of Philip (1972) provides a link between the resulting effective slip length, l_s, and the geometrical structure of the surface pattern, L and Φ:

$$\frac{l_s}{L} = \frac{-1}{\pi} \log\left[\cos\left\{\frac{\pi}{2}(1-\Phi)\right\}\right]. \tag{3.1}$$

The DNS results for the effective slip lengths determined by the time- and space-averaged turbulent flow according to

$$u_s = l_s \left(\frac{\partial \overline{u}}{\partial y}\right)_w \tag{3.2}$$

are compared with this solution. Note that for CPG conditions, it holds that $l_s = u_s$ since the wall shear stress is fixed: $(\partial\overline{u}/\partial y)_w = 1$. It can be seen in figure 5 that for $L \leqslant 35$ laminar and turbulent solutions coincide within the accuracy of the DNS predictions (error bars are included for the two smallest L values according to the estimation shown in figure 4) indicating that l_s is mainly a function of the geometrical properties of the streamwise grooves and does not depend on the flow state. For $L > 35$ significant deviations appear, such that turbulent flow conditions result in lower values of l_s. This difference becomes more pronounced as L increases and indicates the existence of specific turbulent losses, which are analysed further in § 4.2.

3.2. *Relative flow rate increase*

In general, the presence of a SHS increases the bulk mean velocity compared with a channel flow with no-slip walls at the same friction Reynolds number (CPG condition) and constant channel height. The performance of SHS is thus evaluated based on the relative increase of flow rate expressed in terms of the relative increase of the bulk velocity, i.e. $\Delta U_b/U_{b,0}$, where $\Delta U_b = U_b - U_{b,0}$ and the subscript 0 indicates the reference value with no-slip walls.

Figure 6 shows the relative increase in flow rate as a function of the different geometric wavelengths, L, of the grooved surface structure. The DNS results for turbulent flows show that this gain constantly increases with increasing L initially but levels off for values above $L \approx 100$ approaching a maximum increase in flow rate of approximately 50 % for $\Phi = 0.5$. In comparison with l_s, plotted in figure 5, the increase of ΔU_b is slower with increasing L, indicating that additional losses are at play here. These are discussed in § 4.3. The apparent limit of the achievable increase

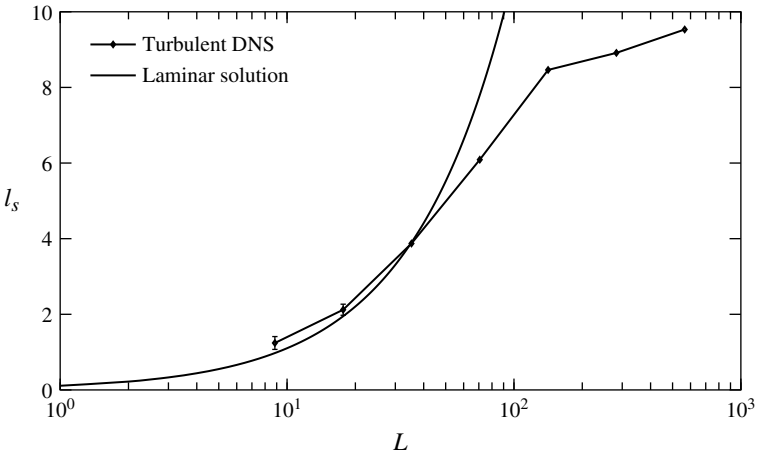

FIGURE 5. Comparison of the effective slip length obtained by DNS of turbulent flows under CPG and the laminar solution of Philip (1972).

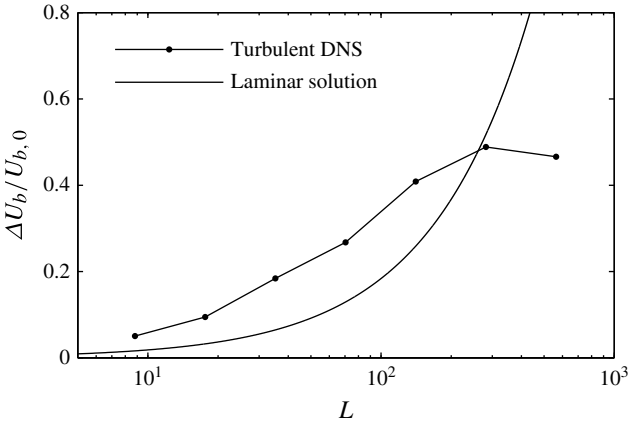

FIGURE 6. Gain in terms of the relative increase in U_b for streamwise grooves at $\Phi = 0.5$ compared with the no-slip reference channel.

in flow rate is particular for turbulent flows. The expected gain under laminar flow conditions can be obtained from (3.1) as follows:

$$\left(\frac{\Delta U_b}{U_{b,0}}\right)_{lam} = \frac{\dfrac{-L}{\pi}\log\left[\cos\left\{\dfrac{\pi}{2}(1-\Phi)\right\}\right]}{Re_\tau/3} - 1 \tag{3.3}$$

and is also included in figure 6. As already noted by Daniello *et al.* (2009), it can be seen that at low values of L, SHS are more effective under turbulent conditions than under laminar ones. For large values of L the opposite is true since the turbulent losses outweigh the benefit of higher near-wall velocity gradients in turbulent flow.

3.3. *Velocity statistics over SHS*

The spatial mean velocity profiles for different L are plotted in figure 7(*a*). The general shape of the velocity profile found above purely no-slip walls is maintained with

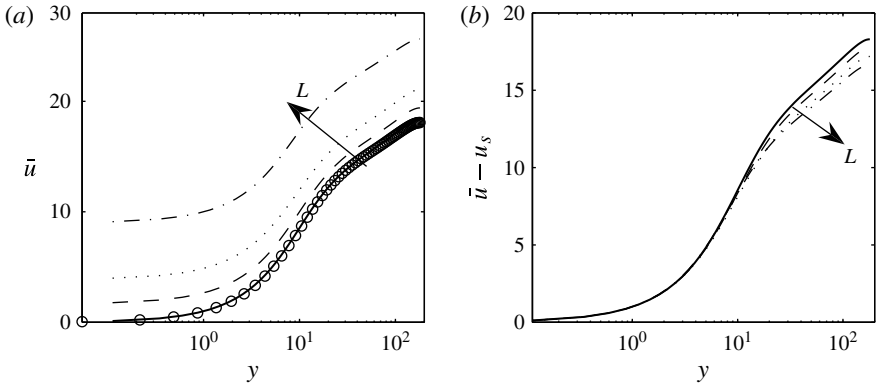

FIGURE 7. Mean streamwise velocity profiles (*a*) as obtained from the simulation and (*b*) shifted by the corresponding slip velocity for: – –, $L = 8.8$; · · · , $L = 35.2$; – · –, $L = 281.6$; ——, no-slip reference channel; ○, DNS from Kim *et al.* (1987). The arrow indicates an increase in L.

an offset at the wall that corresponds to the effective slip velocity. If the profiles are corrected by this offset, they collapse within the viscous sublayer as shown in figure 7(*b*). This collapse is expected, since the average velocity gradient at the wall is fixed under the CPG condition. In the channel centre such a collapse of the velocity profiles is not found. The relative velocity decreases with increasing L. As pointed out above, this reduction is particular for turbulent flows and is not found under laminar conditions. The same trend is observed when a uniform slip length in streamwise and spanwise direction is prescribed at the wall. This change of the relative mean velocity profile is generally linked to an increase of turbulence activity which Min & Kim (2004) relate to slip effects in the spanwise direction.

In contrast to the spatial mean velocity profile, the phase resolved streamwise velocity, $\langle u \rangle$, which can be seen in the contour plots of figures 12 and 14 clearly reflects the numerical representation of streamwise grooves. In order to enable a comparison of the statistics for flows over streamwise grooves with those for a prescribed homogeneous slip length the split-up into a coherent and random part as introduced in § 2.3 is applied in the following.

The Reynolds stresses for different L are shown in figures 8–11. The non-homogeneity of the boundary condition in spanwise direction has the largest effect on the streamwise component of the Reynolds stresses, $\overline{u'^2}$. The coherent contribution, $\overline{\tilde{u}^2}$, increases with increasing L and decreases with increasing wall distance. The increase with L is due to the fact that higher velocities can develop along a wider groove, i.e. the free-slip surface. The coherent contributions to $\overline{\tilde{v}^2}$ and $\overline{\tilde{w}^2}$ are small for small L but increase for the two largest wavelengths, suggesting the presence of a secondary flow. This observation is analysed in § 3.4 in more detail.

The random contributions to the normal stresses show non-zero values of $\overline{u''^2}$ and $\overline{w''^2}$ at the wall due to the local no-shear condition while $\overline{v''^2}$ has to approach zero due to non-permeability of the boundary. In general, an increase of the peak value for the random part of the normal Reynolds stresses and a slight shift of its location towards smaller wall distances can be observed for SHS in comparison with no-slip walls.

In contrast to these results, Min & Kim (2004) report decreasing peak values of the normal stresses for combined streamwise and spanwise slip. As already discussed with

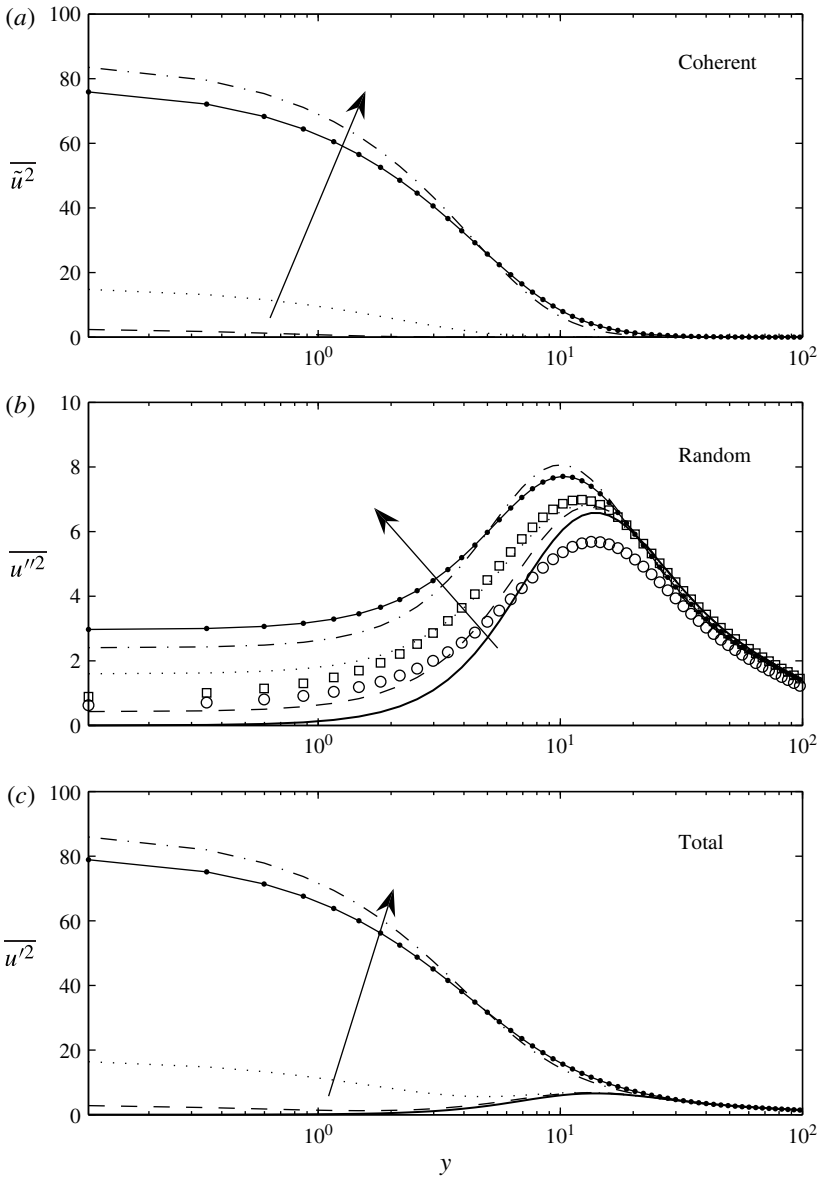

FIGURE 8. Streamwise component of the normal Reynolds stresses for: – –, $L = 8.8$; · · · , $L = 35.2$; –●–, $L = 140.8$; – · –, $L = 281.6$; ○, CFR homogeneous partial slip; □, CPG homogeneous partial slip; ——, no-slip reference channel. The arrow indicates the direction of increasing L. The total Reynolds stress ($\overline{u'^2}$) is given by the sum of the coherent ($\overline{\tilde{u}^2}$) and the random ($\overline{u''^2}$) contribution.

respect to figure 2, this discrepancy is primarily caused by the simulation strategy and not by the way the SHS is modelled. The data for combined homogeneous partial slip under CFR and CPG are therefore included in the middle part of figure 8 for reference. The slip length, l_s, corresponds approximately to the value obtained for $L = 35.2$ and it can be seen that the statistics for random velocity fluctuations in streamwise direction

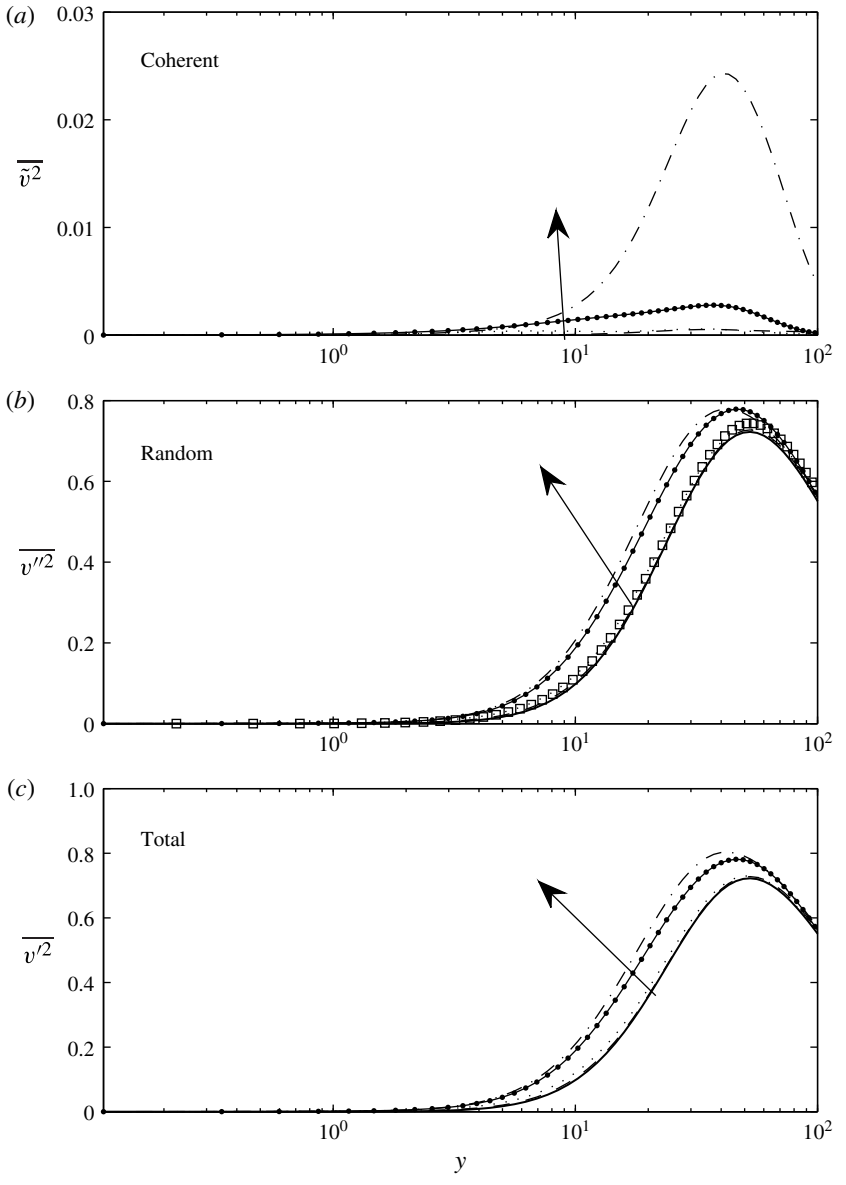

FIGURE 9. Wall-normal component of the normal Reynolds stresses for: −−, $L = 8.8$; · · · , $L = 35.2$; -●- , $L = 140.8$; − · −, $L = 281.6$; □, CPG homogeneous partial slip; ——, no-slip reference channel. The arrow indicates the direction of increasing L.

are similar for $y > 13$ for the two CPG cases. However, clear differences can be seen in the near-wall region where $\overline{u''^2}$ is larger for the case with streamwise grooves than for that with homogeneous partial slip. This difference can be linked to the fact that $\overline{u''^2}$ is mainly generated over the free-slip region of the streamwise grooves where the local slip length is infinite. The uniform slip length model is a macroscopic model, which ignores the inhomogeneity of the local surface boundary condition, so that it is expected that the uniform slip length model fails to predict turbulence statistics near

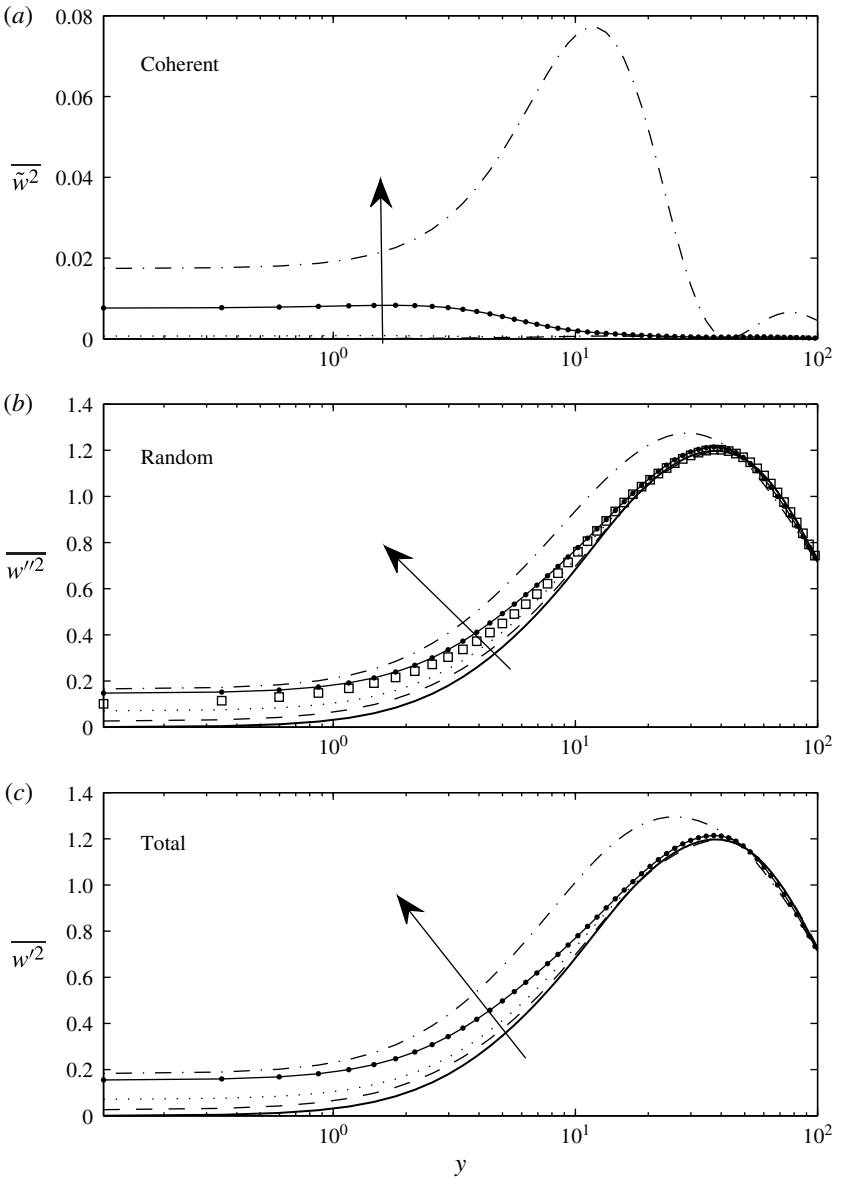

FIGURE 10. Spanwise component of the normal Reynolds stresses for: −− $L = 8.8$; ⋯ , $L = 35.2$; -●- , $L = 140.8$; − · −, $L = 281.6$; □, CPG homogeneous partial slip; ——, no-slip reference channel. The arrow indicates the direction of increasing L.

the SHS, especially at large L. However, it should be emphasized that such a simple model can well reproduce the trend of turbulence statistics away from the wall as shown in the middle plot of figure 8, if the uniform slip length is properly given. A very good agreement between the two simulation approaches is also found for the random part of the Reynolds shear stress, as shown in figure 11, when the same l_s is realized.

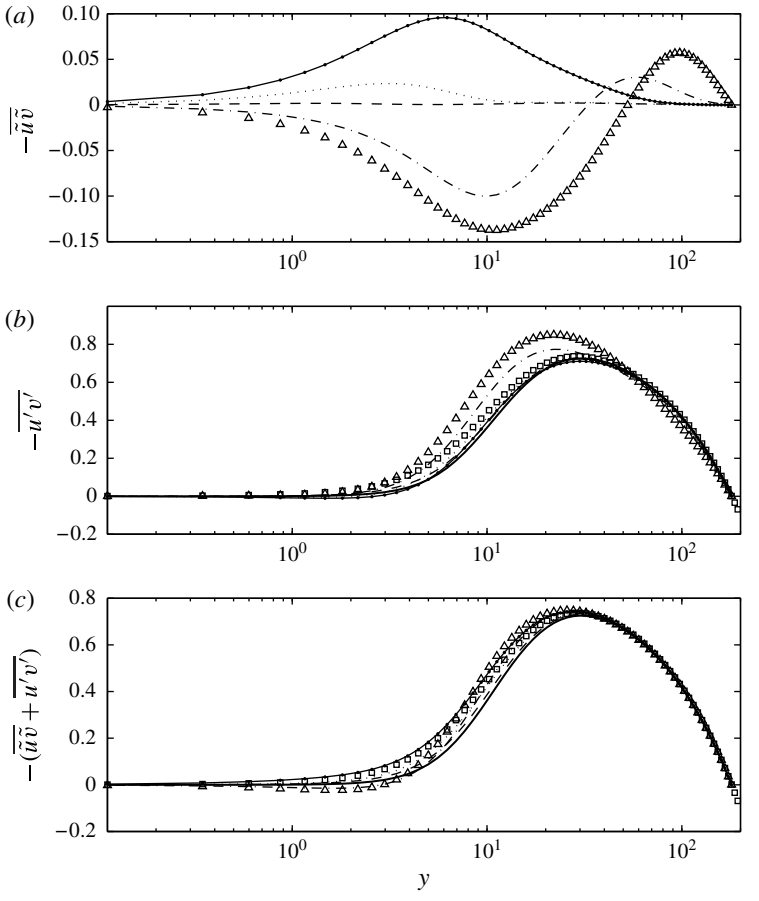

FIGURE 11. Reynolds shear stress for: −−, $L = 8.8$; ⋯ , $L = 35.2$; -●- , $L = 140.8$; −·−, $L = 281.6$; △, $L = 563.2$; □, CPG homogeneous partial slip; ——, no-slip reference channel.

The random spanwise fluctuations $\overline{w''^2}$ increase with increasing L, except for the centre region of the channel, where they remain largely unchanged up to $L = 140.8$. The CPG data for homogeneous partial slip are obtained with the same prescribed partial slip in streamwise and spanwise direction. In contrast to the streamwise direction a direct comparison of $\overline{w''^2}$ obtained with partial slip and with one specific L-value is not possible since there is no clear definition available for the effective spanwise slip length, l_s^z. Estimations of l_s^z based on $\overline{w''^2}$ or the corresponding root-mean-square (r.m.s.) value are difficult due to the very small and spatially varying near-wall gradient. As already pointed out with respect to $\overline{u''^2}$ the overall trend for $\overline{w''^2}$ (and also for $\overline{v''^2}$) are well captured with the homogeneous slip model.

The total Reynolds shear stress, as shown in figure 11, generally increases with increasing L. However, a saturation of this effect can be observed. The coherent contribution, which indicates the presence of a secondary flow structure, is generally smaller than the random contribution but shows the interesting fact of a reversed sign for the two largest wavelengths: negative values of $-\overline{\tilde{u}\tilde{v}}$ appear.

3.4. *Secondary flow*

The existence of non-negligible coherent contributions to $\overline{v'^2}$ and $\overline{w'^2}$ at larger wavelengths L indicate the presence of secondary flow structures. Careful data analysis shows that secondary flow structures of Prandtl's second kind (Nikuradse 1926; Pöschl 1926), i.e. in the form of streamwise vortices, are indeed present for all investigated values of L. Figure 12 shows the secondary motion in the y–z plane for $L = 17.6$, 140.8 and 281.6. The underlying contour plot of the streamwise velocity reflects the fact that the flow rate in the channel increases with increasing L, i.e. from $U_b = 17.1$ for $L = 17.6$ to $U_b = 23.3$ for $L = 281.6$. The secondary motion consists of a pair of counter-rotating vortices which extend roughly one wavelength in wall-normal direction for small L and cover the entire channel height when the ratio L/δ approaches one. The trend in the strength of the secondary motion can be deduced from the coherent parts of figures 9 and 10: it increases with increasing L. For the lower values of L the vortical motion transports fluid downwards over the free-slip area and upwards over the no-slip area. Interestingly, for the two largest wavelengths considered a secondary motion with opposite rotational direction is observed. Namely, a downwelling motion occurs over the no-slip area, while the upwelling is located above the free-slip area. Since $\tilde{u}$ is always positive near the free-slip area regardless of the value of L, this reversed vorticity leads to the change of sign for the coherent part of the Reynolds shear stress as observed in figure 11.

In order to further investigate the mechanism and the dynamics of the secondary flow over SHS, we consider the transport equation for the phase averaged streamwise vorticity $\langle\omega_x\rangle$:

$$\langle v\rangle \frac{\partial \langle\omega_x\rangle}{\partial y} + \langle w\rangle \frac{\partial \langle\omega_x\rangle}{\partial z} = -\frac{\partial^2 \langle w''v''\rangle}{\partial y^2} - \frac{\partial^2 \langle w''w''\rangle}{\partial y \partial z} + \frac{\partial^2 \langle v''v''\rangle}{\partial y \partial z} + \frac{\partial^2 \langle v''w''\rangle}{\partial z^2} + \frac{1}{Re_\tau}\left(\frac{\partial^2 \langle\omega_x\rangle}{\partial y^2} + \frac{\partial^2 \langle\omega_x\rangle}{\partial z^2}\right). \tag{3.4}$$

The terms on the left-hand-side represent the convection of $\langle\omega_x\rangle$ due to the secondary flow. The first four terms on the right-hand-side are production terms of $\langle\omega_x\rangle$, while the last term represents the viscous diffusion of $\langle\omega_x\rangle$. Considering that the convection and diffusion terms do not produce vorticity, it is required that the production terms have non-zero value in order to generate secondary motion. The production terms include either a derivative in spanwise direction or the correlation $\langle v''w''\rangle$ such that non-zero values can only be obtained when the alternating no-slip and no-shear surfaces are resolved. Therefore, the effective slip model as introduced by Min & Kim (2004), which is homogeneous in the spanwise direction, cannot lead to the formation of secondary flow.

The production of $\langle\omega_x\rangle$ is largest close to the boundary between free-slip and no-slip regions. Its spatial extent in the spanwise direction is around $\Delta z \approx 10$ and almost independent of L. For $L < 140$ the two neighbouring secondary vortices with opposite sign force the flow upward above the no-slip area and downward over the free-slip region as shown sketched in figure 13(*a*). For larger L the same production mechanism seems to act at the interface between the no-slip and the free-slip wall. In this case, however, the extension of the locally induced vortices is much smaller than their spanwise separation. Thus, they do not interact directly but induce an additional tertiary vortical motion at larger wall distance as sketched in figure 13(*b*).

The fact that secondary vortices are produced at the interface between the no-slip and the free-slip wall and generate tertiary vortices depending on the distance between

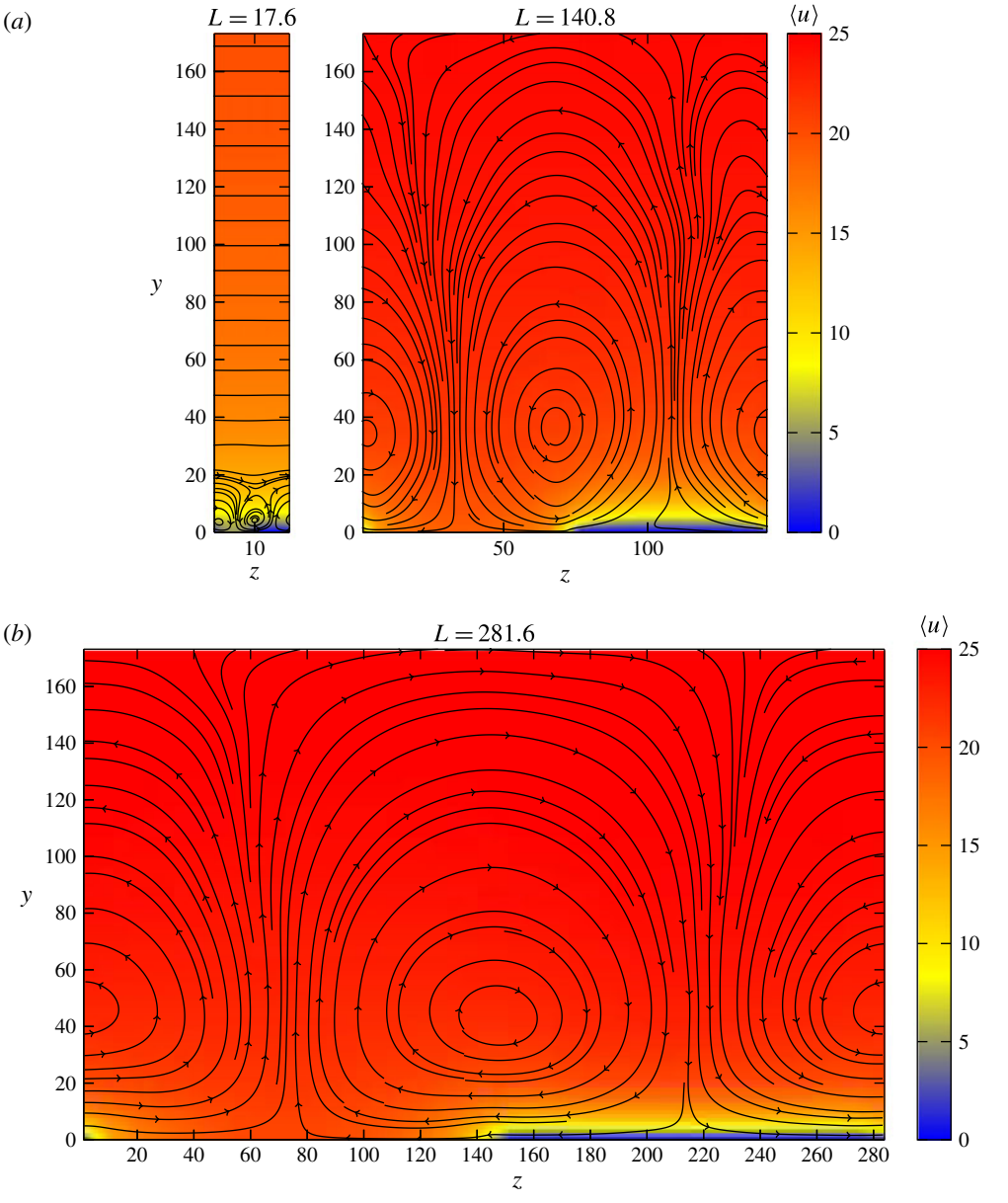

FIGURE 12. Visualization of the secondary flow in the y–z-plane with superimposed colour contour of the phase-resolved streamwise velocity, $\langle u \rangle$.

the interfaces can also be observed if a variation of the solid fraction is considered. Figure 14 shows the streamlines of the induced vortical structures for $\Phi = 0.25$ and $\Phi = 0.75$ in the y–z plane. There is a downwelling motion above the free-slip region close to the interface. For large free-slip areas, here $\Phi = 0.25$, a tertiary vortex with opposite rotational direction is induced which causes an upwelling motion above the centre of the free-slip area.

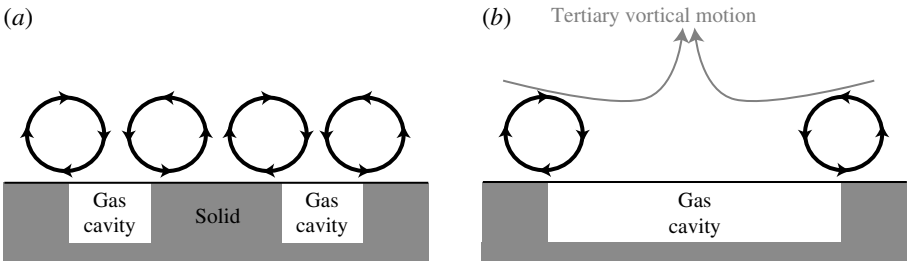

FIGURE 13. Schematic of the secondary flow mechanism over a SHS with (*a*) small and (*b*) large groove widths.

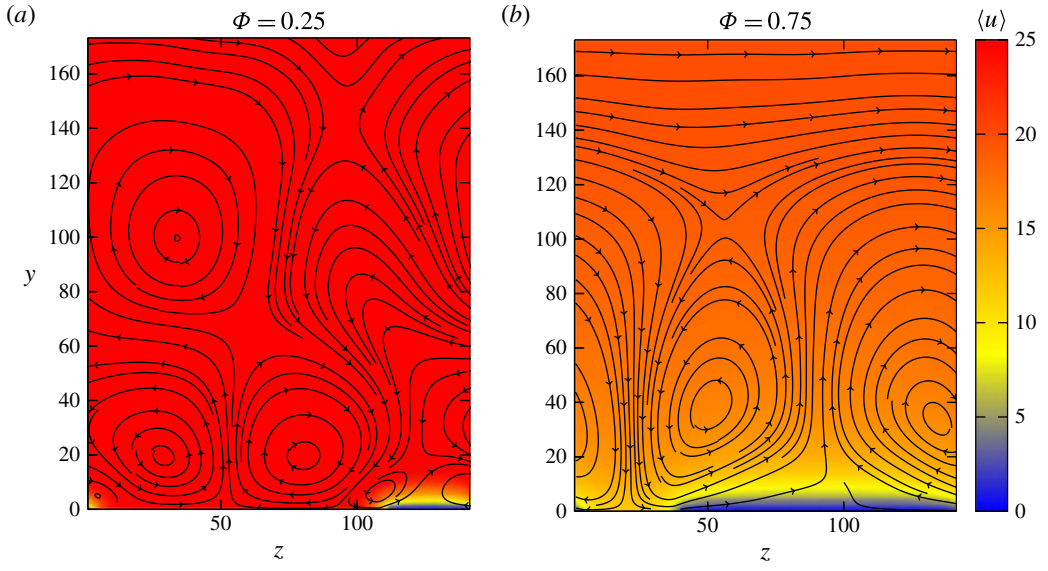

FIGURE 14. Visualization of the secondary flow in the y–z-plane with superimposed colour contour of the phase-resolved streamwise velocity, $\langle u \rangle$, for $L = 140.8$ with different solid fractions.

A similar observation, i.e. that periodically varying surface structures induce a secondary motion in the form of streamwise-oriented vortices, is known from Goldstein & Tuan (1998) who report secondary flows in turbulent flow over riblets if a certain riblet spacing is exceeded. The strength of the secondary flow increases with increasing riblet spacing. For very large riblet spacing they observe the existence of tertiary vortices which are induced by the secondary flow motion which is consistent with the present observations.

4. Mechanism of the flow rate increase and its estimation

4.1. *Mathematical relationship between the flow rate and different dynamical contributions*

In order to quantify the importance of the different mechanisms that determine the flow rate increase over SHS, the approach of Fukagata *et al.* (2002) and Marusic,

Joseph & Mahesh (2007), who present a mathematical relationship between the wall friction and different dynamical contributions in wall-bounded flows, is extended for a SHS. Applying triple integration to the averaged transport equation for the streamwise momentum under the assumption of a CPG and symmetry of the flow with respect to the channel centreline, results in the following identity, which is also presented in similar form in Hasegawa, Frohnapfel & Kasagi (2011):

$$U_b = \frac{Re_\tau}{3} + u_s - \int_0^\delta \left(1 - \frac{y}{\delta}\right) \left(-\overline{u'v'}\right) \, \mathrm{d}y. \tag{4.1}$$

The first term on the right-hand side corresponds to the laminar flow rate over a no-slip surface under the same pressure gradient. This laminar contribution is constant since Re_τ is fixed. Hence, the flow rate is determined by the second and third terms on the right-hand side of (4.1). The second term represents the contribution of the slip velocity, u_s ($= l_s$ for CPG conditions), and the third term is that of the weighted Reynolds shear stress, which basically reflects the shape of the velocity profile. In a laminar flow, the turbulence contribution is absent, so that the increase in flow rate is determined solely by the slip velocity. In turbulent flows, however, the third term leads to a significant reduction of the bulk velocity.

For the reference case of a flow over no-slip walls, denoted by the subscript of 0, equation (4.1) reduces to

$$U_{b,0} = \frac{Re_\tau}{3} - \int_0^\delta \left(1 - \frac{y}{\delta}\right) \left(-\overline{u_0'v_0'}\right) \, \mathrm{d}y. \tag{4.2}$$

Since we are interested in the differences between purely no-slip surfaces and SHS, we subtract (4.2) from (4.1) so that

$$\Delta U_b = U_b - U_{b,0} = u_s - \underbrace{\int_0^\delta \left(1 - \frac{y}{\delta}\right) \left(-\overline{u'v'} + \overline{u_0'v_0'}\right) \, \mathrm{d}y}_{\text{additional turbulent losses } \Delta U_{loss}}. \tag{4.3}$$

Figures 15 and 16 show the change in bulk velocity, ΔU_b, and its contributions as given by (4.3) for different L and Φ. It can be seen that the change in U_b is mainly governed by the slip velocity, u_s. Since $u_s = l_s$, this curve corresponds to the one for l_s plotted in figure 5. The reduction of U_b due to the additional turbulent losses, ΔU_{loss}, seems to saturate with increasing L. This saturation is also reported in other numerical studies that are based on uniform spanwise slip length (Fukagata *et al.* 2006; Busse & Sandham 2012). In the following we analyse both contributions that determine the effectiveness of the SHS with streamwise grooves in a turbulent flow, namely, the effective slip length, l_s, and the additional turbulent losses, ΔU_{loss}, in more detail.

4.2. *Effective slip in turbulent flow*

The potential reasons that lead to the observed saturation of l_s or u_s in turbulent flows can be analysed by considering the transport equation of the phase-averaged streamwise velocity $\langle u \rangle$:

$$\langle v \rangle \frac{\partial \langle u \rangle}{\partial y} + \langle w \rangle \frac{\partial \langle u \rangle}{\partial z} = -\frac{\partial \langle u''v'' \rangle}{\partial y} - \frac{\partial \langle u''w'' \rangle}{\partial z} - \frac{\partial \langle p \rangle}{\partial x} + \left(\frac{\partial^2 \langle u \rangle}{\partial y^2} + \frac{\partial^2 \langle u \rangle}{\partial z^2} \right). \tag{4.4}$$

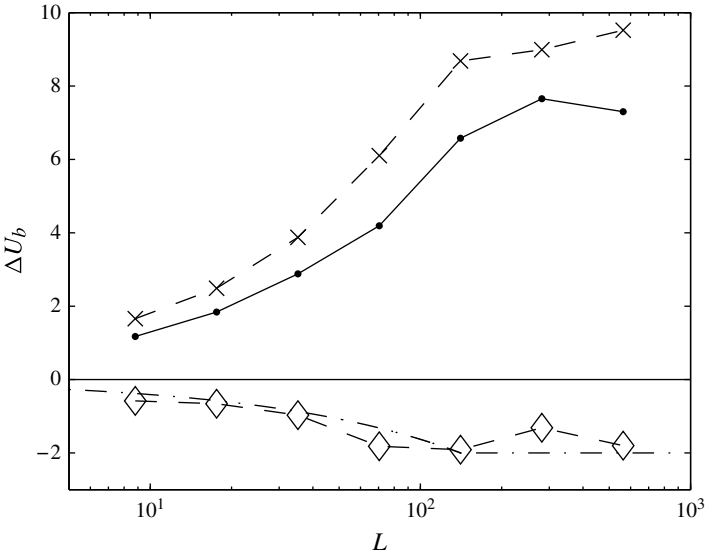

FIGURE 15. Contributions to the change of the bulk velocity according to (4.3) for different L at $\Phi = 0.5$: ●, ΔU_b; ×, u_s; ◇, ΔU_{loss}; – · –, values predicted for ΔU_{loss} according to (4.12) and (4.13).

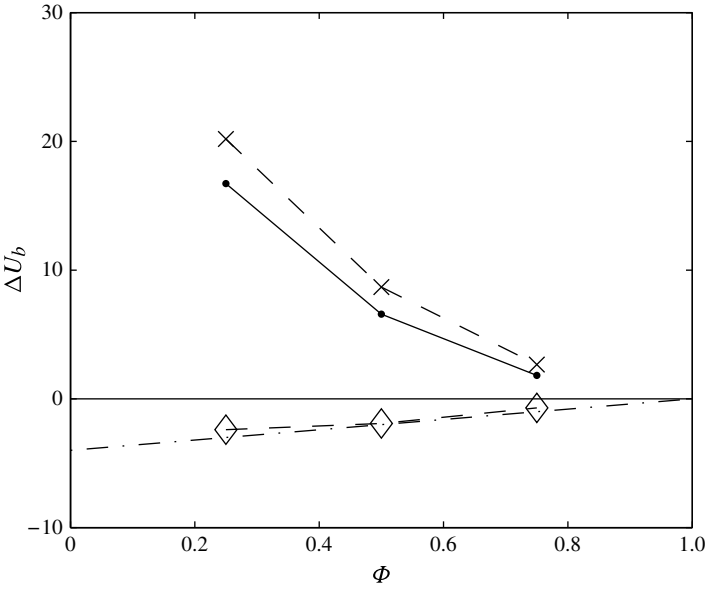

FIGURE 16. Contributions to the change of the bulk velocity according to (4.3) for different Φ at $L = 140.8$: ●, ΔU_b; ×, u_s; ◇, ΔU_{loss}; – · –, values predicted for ΔU_{loss} according to (4.12).

Note that $-\partial \langle p \rangle / \partial x = 1/Re_\tau = const.$ in the present configuration. The two terms on the left-hand side represent the convective transport by the phase-averaged flow, i.e. the secondary flow. The first two terms on the right-hand side arise from the

Reynolds shear stresses, and correspond to turbulent diffusion, while the last term expresses the viscous diffusion of $\langle u \rangle$. In laminar flow, the terms related to the secondary flow (convective transport) and the turbulent diffusion are not present. Hence, one of them (or both) should cause the deviation of l_s from Philip's laminar solution at larger L as shown in figure 5.

In order to consider the effect of turbulent diffusion, we introduce the turbulent (eddy) viscosity ν_t as

$$-\left\langle u_i'' u_j'' \right\rangle \approx \nu_t \left(\frac{\partial \langle u_i \rangle}{\partial x_j} + \frac{\partial \langle u_j \rangle}{\partial x_i} \right). \tag{4.5}$$

By substituting (4.5) into (4.4), we obtain

$$\langle v \rangle \frac{\partial \langle u \rangle}{\partial y} + \langle w \rangle \frac{\partial \langle u \rangle}{\partial z} = -\frac{\partial \langle p \rangle}{\partial x} + \frac{\partial}{\partial y} \left\{ (1+\nu_t) \frac{\partial \langle u \rangle}{\partial y} \right\} + \frac{\partial}{\partial z} \left\{ (1+\nu_t) \frac{\partial \langle u \rangle}{\partial z} \right\}. \tag{4.6}$$

In general, ν_t is a local property of turbulence, and therefore a function of y and z. The simplest approach is to assume that ν_t is identical to that over a no-slip surface. In this case, ν_t is a function of y only and its empirical expression is given by Reynolds & Hussain (1972):

$$\nu_t = \frac{\nu_t^*}{\nu^*} = \frac{1}{2} \left[1 + \left\{ \frac{\kappa Re_\tau}{3} \left(1-y^2\right) \left(1+2y^2\right) \left(1 - \exp\left[-\frac{(1-|y|)Re_\tau}{A} \right] \right) \right\}^2 \right]^{-1/2} - \frac{1}{2}. \tag{4.7}$$

Here, κ and A are empirical constants, usually set to $\kappa = 0.426$ and $A = 26$. Note that in (4.7), the locations of top and bottom walls correspond to $y = -1$ and 1, and the channel centre is at $y = 0$. In the above equation, A is the van Driest constant which represents the attenuation of turbulence due to the presence of a solid surface. In the case of a SHS this value should be changed in order to reflect the modified boundary conditions. For a free-slip surface the van Driest constant can be estimated to $A_{fs} = 13.9$ by fitting (4.7) to the DNS data of Hasegawa & Kasagi (2007) using the method of nonlinear least squares. When the same fitting procedure is applied to the no-slip reference channel data a value of $A_{ns} = 25.8$ is obtained which is in a good agreement with the conventionally known value of $A = 26$ (Van Driest 1956).

In order to estimate the van Driest constant at a SHS we employ the weighted sum of A_{fs} and A_{ns} according to

$$A_{SHS} \approx \Phi A_{ns} + (1-\Phi) A_{fs}. \tag{4.8}$$

Figure 17 shows a comparison of this simple model prediction with the eddy viscosity profiles extracted from the present DNS data for different Φ at $L = 140.8$. Since the agreement is reasonable we use (4.7) with A_{SHS} as given by (4.8) for modelling ν_t over a SHS in the following.

Once ν_t is fixed (4.6) can be solved in the y–z plane with the same boundary conditions that are used in the DNS. In order to evaluate the convective transport terms due to secondary motion, i.e. the left-hand side of (4.6), the information of $\langle v \rangle$ and $\langle w \rangle$ has to be provided. In the present calculation, they are extracted from the DNS data. In order to clarify the importance of these terms, an additional computation without the secondary flow is carried out by setting the left-hand-side of (4.6) to zero.

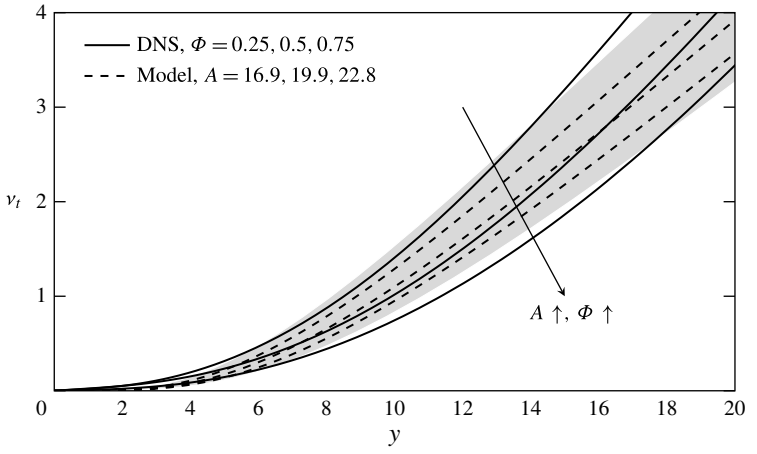

FIGURE 17. Comparison of turbulent viscosity profiles from DNS simulations with modelled profiles at $L = 140.8$. The grey shaded area represents an array of possible viscosity distributions according to (4.8) between the boundaries of a free-slip surface, $A_{fs} = 13.9$, and a no-slip wall, $A_{ns} = 25.8$.

The resulting slip length, $l_s = u_s$, is obtained by the spatial average of $\langle u \rangle$ at the SHS. The results for varying L and Φ, based on a spanwise resolution of $\Delta z = 2.2$, are shown in figures 18 and 19, respectively, in comparison with the DNS data. The comparison of the model results with and without consideration of the secondary flow reveals that the tertiary vortices observed for $L = 281.6$ and 563.2 at $\Phi = 0.5$ have a significant impact on l_s while the influence of 'pure' secondary motions is rather weak. The same conclusions can be drawn based on the results presented in figure 19: the initial deviation of l_s from the laminar solution is mainly caused by the enhanced momentum transfer under turbulent flow conditions; once tertiary vortices appear (in this case for $L = 140.8$ at $\Phi = 0.25$) their presence strongly influences l_s.

In order to use these results for the development of a modelling strategy for l_s, the analytical solution for laminar flow is sketched additionally in figures 18 and 19. Obviously, its agreement with the DNS data is excellent for small L in the case of $\Phi = 0.5$. For $L > 35.2$, however, the prediction of l_s taking turbulent diffusion into account according to (4.7) clearly increases the quality of the results. Only for very large L, for which tertiary vortices appear, the proposed model starts to fail. Similar conclusions can be drawn for the variation of Φ. Comparison of the results with varying L and Φ suggests, that the recommended prediction method for l_s strongly depends on the width of the no-slip boundary, $(1 - \Phi)L$: based on the results presented, it is expected that the analytical solution provides good results for approximately $(1 - \Phi)L < 20$, the simple model based on the introduction of a turbulent viscosity seems to be applicable up to roughly $(1 - \Phi)L = 75$.

4.3. *Additional turbulent losses*

The additional turbulent losses in (4.3) can be further decomposed into coherent and random contributions as

$$\Delta U_{loss} = \underbrace{\int_0^{\delta} \left(1 - \frac{y}{\delta}\right) \left(-\overline{u''v''} + \overline{u''_0 v''_0}\right) \mathrm{d}y}_{I} + \underbrace{\int_0^{\delta} \left(1 - \frac{y}{\delta}\right) \left(-\overline{\tilde{u}\tilde{v}}\right) \mathrm{d}y}_{II}. \tag{4.9}$$

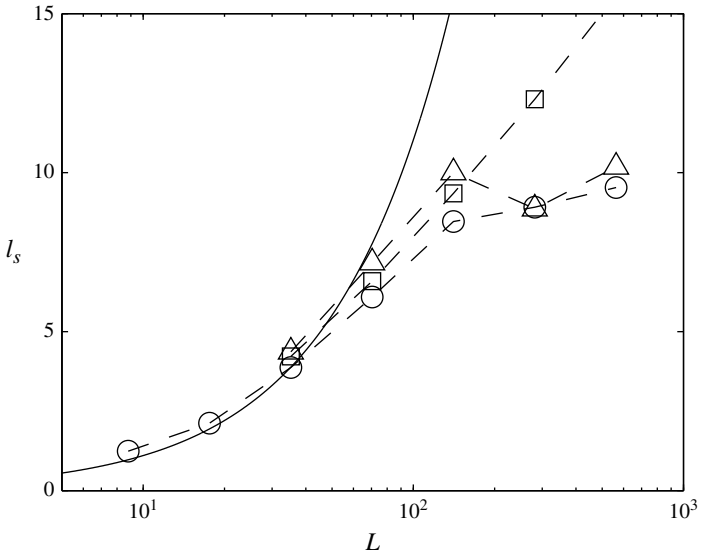

FIGURE 18. Comparison of the effective slip length obtained in DNS and predicted by the present model (4.6) for different L at $\Phi = 0.5$: ●, DNS; —-, laminar solution from Philip (1972); □, model without secondary flow; △, model with secondary flow pattern (extracted from DNS).

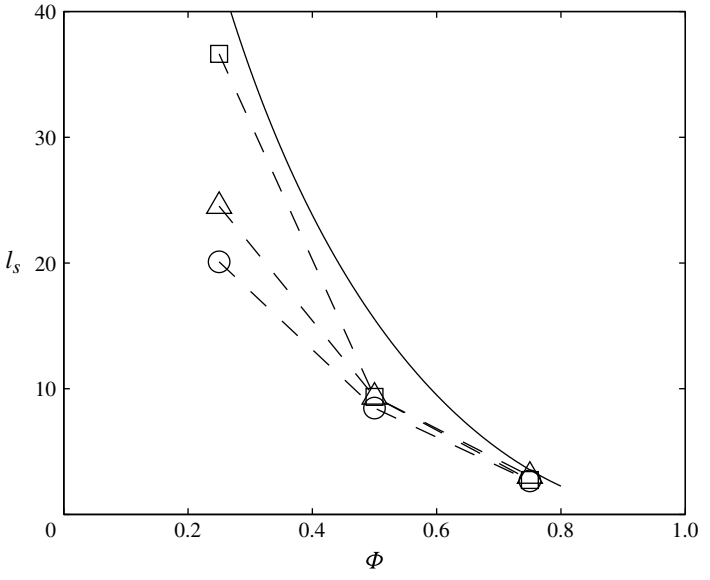

FIGURE 19. Comparison between the effective slip lengths obtained in DNS and predicted by the present model (4.6) for different Φ at $L = 140.8$: ●, DNS; —, laminar solution from Philip (1972); □, model without secondary flow; △, model with secondary flow pattern (extracted from DNS).

Here, I is the reduction of the bulk mean velocity due to the random part of the Reynolds shear stress and II is the contribution due to its coherent part. Note that the coherent contribution vanishes for a purely no-slip surface.

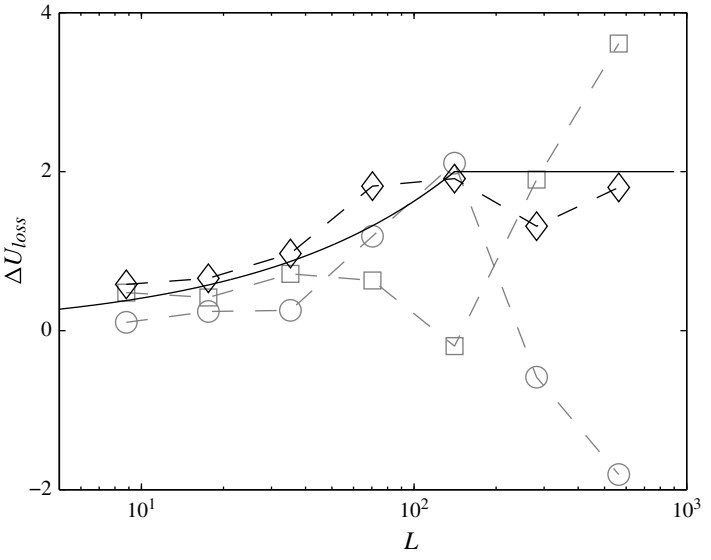

FIGURE 20. Contributions to ΔU_{loss} according to (4.9) for different L: ◇, $\Delta U_{loss} = I + II$; □, random contribution I; ●, coherent contribution II; —-, values predicted for ΔU_{loss} according to (4.12) and (4.13).

In figure 20, the coherent and random contributions and also their sum are plotted as a function of L at $\Phi = 0.5$. It is observed that the coherent and random contributions to the bulk mean velocity change irregularly with increasing L. Specifically for the two largest L, the coherent contribution changes its sign, so that it contributes to an increase of the flow rate. Meanwhile, the turbulent loss arising from the random component is drastically enhanced. This change can be attributed to the change of the rotation direction of the secondary motion as discussed in § 3.4. Although there remain open questions on how the large-scale secondary motion influences the random fluctuating fields, previous studies such as Schoppa & Hussain (1998) and Fukagata, Kobayashi & Kasagi (2010) suggest a strong interaction between them. Despite the complex behaviour of the coherent and random contributions, their changes balance, so that the total turbulent loss changes rather gradually. Namely, it monotonically increases with increasing L and then saturates. This trend is similar to the additional turbulent losses observed in previous DNS assuming homogeneous spanwise slip on the wall. Accordingly, we consider the total value of ΔU_{loss} in the following and develop a model following existing empirical formulas established for SHS with a prescribed homogeneous spanwise slip length, l_s^z.

Fukagata *et al.* (2006) estimate the additional turbulent losses due to l_s^z in their DNS data to

$$\Delta U_{loss} = 4[1 - \exp(-(l_s^z/7)^{0.7})]. \tag{4.10}$$

This relation is reconsidered by Busse & Sandham (2012). Using data from an extensive parametric study for different combinations of streamwise and spanwise slip lengths they propose ΔU_{loss} to be more accurately presented by

$$\Delta U_{loss} = 4\left(1 - \frac{4}{4 + l_s^z}\right). \tag{4.11}$$

Both correlations yield a limit for the additional turbulent losses due to homogeneous spanwise slip of $\Delta U_{loss,max} = 4$. In the present investigation, the spanwise slip is not given through a prescribed value for l_s^x, but results from the geometrical properties of the surface pattern. By simply introducing the ratio of free surface area, Φ, a as a weighting factor such that

$$\Delta U_{loss,max} \approx 4\,(1-\Phi)\,, \tag{4.12}$$

a limit for ΔU_{loss} for non-homogeneous spanwise slip can be estimated. For $\Phi = 0.5$, this results in $\Delta U_{loss,max} = 2$ which is in reasonable agreement with results for larger values of L in figure 15. Also for the additional Φ-values considered at $L = 140$ the corresponding agreement is good.

In order to use (4.11) in the design process of a SHS a connection between l_s^x and L would be required. However, the evaluation of an effective spanwise slip length is not possible analogue to (3.2) as there is no mean flow in the spanwise direction. Since the present simulations at $Re_\tau = 180$ and $L = 140.8$ show good agreement with the estimated $\Delta U_{loss,max}$ and the increase of ΔU_{loss}, when approaching this L value, is similar to that for u_s, i.e. $\propto L^{0.6}$ for the present data (see figure 15), a rough estimate for ΔU_{loss} can be given by

$$\Delta U_{loss} \approx 4\,(1-\Phi)\left(\frac{L}{140.8}\right)^{0.6}, \tag{4.13}$$

for $L < 140.8$. This trend is in reasonable agreement with the present data shown in figure 15, but further numerical results for a range of surface structures and Reynolds numbers are required to confirm that such an estimation is indeed possible.

4.4. *Estimation of the flow rate increase*

As shown in (4.3), the gain of a SHS is given by the sum of $u_s = l_s$ and $-\Delta U_{loss}$, and their modelling strategies are presented in the preceding §§ 4.2 and 4.3. Here, these models are combined in order to compare the model prediction for the flow rate increase with the current DNS results. For the following estimations we consider groove widths of $L < 150$ at $\Phi = 0.5$ for which the effect of the secondary flow on l_s is small and for which (in contrast to very large L values) the stable existence of a flat air–water interface can be assumed (see appendix A).

Figure 21 presents the relative increase of the bulk mean velocity obtained by DNS in comparison with the model prediction. For $L \leqslant 35$, l_s in turbulent flows can be extracted from Phillip's analytical laminar solution. Therefore, the prediction of ΔU_b is based on the laminar solution (3.3) in combination with the model for ΔU_{loss} (4.13). Since it is shown in § 4.1 that the influence of ΔU_{loss} on ΔU_b is relatively small the corresponding curve based on solely the analytical solution for l_s is also included. Although good agreement with the DNS data can only be expected for $L \leqslant 35$, the corresponding results over the entire L range are plotted in figure 21 for reference. For larger L, not only l_s but also ΔU_b can directly be extracted from the solution of (4.6) for which the left-hand side is set to zero (see § 4.2). Therefore, a separate model for ΔU_{loss} is not required. Overall, it is found that the model overestimates the gain in flow rate due to SHS for larger values of L. However, the agreement is reasonable considering the simple underlying model formulation.

The present model does not require any numerical computations for $L \leqslant 35$ and only a two-dimensional laminar computation for larger values of L (as long as no tertiary

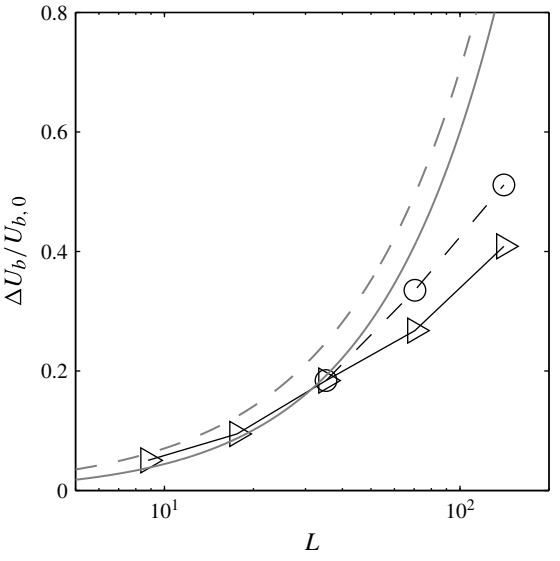

FIGURE 21. Plot of ΔU_b at $Re_\tau = 180$ with $\Phi = 0.5$: model predictions (●) according to the solution of (4.6) in comparison with the DNS data (▷). The grey lines correspond to a prediction of ΔU_b based on solely the analytical solution for l_s in the Stokes regime (dashed line) and in combination with the model for ΔU_{loss} (solid line).

vortices are present). Therefore, it allows the influence of a SHS in turbulent flows to be estimated at practically high Reynolds numbers. Figure 22(*a*) shows the estimation of the slip length at different friction Reynolds numbers of $Re_\tau = 180, 10^3, 10^4, 10^5$. The model predictions for l_s at different Re_τ basically collapse for all L indicating that the effective slip length does not exhibit a Reynolds number dependency in wall units. This behaviour arises from the fact that the turbulent viscosity as introduced in (4.5) is almost independent of Re_τ in the near wall region. Since l_s is independent of Re_τ the relative gain in terms of the predicted increase in flow rate decreases with increasing Reynolds number as shown in figure 22(*b*). At $Re_\tau = 10^5$ the prediction still yields a gain in flow rate of almost 29 % with $L = 140.8$ while it reaches only 13 % for $L = 35$. Considering these results in combination with the reduced stability of the air–water interface at increasing Reynolds number (see appendix A) suggests that a flow rate increase above 10 % is unlikely to be realized with SHS consisting of streamwise grooves at higher Reynolds numbers.

5. Conclusion

We conduct a series of DNS of turbulent flow over a SHS carrying streamwise straight grooves at $Re_\tau = 180$. The SHS is modelled as alternating free-slip and no-slip boundary conditions, the spanwise periodicity L of which is systematically changed in order to investigate its influence on the turbulence dynamics and the resultant gain. In contrast, previous investigations of SHS in turbulent flows often use a homogeneously prescribed slip length. In addition, they compare the obtained results to a no-slip reference channel with the same flow rate (CFR) while the present investigation is carried out for a CPG. In the present paper, it is first shown that significant differences in the obtained results can be attributed to the simulation approach, i.e. whether CFR

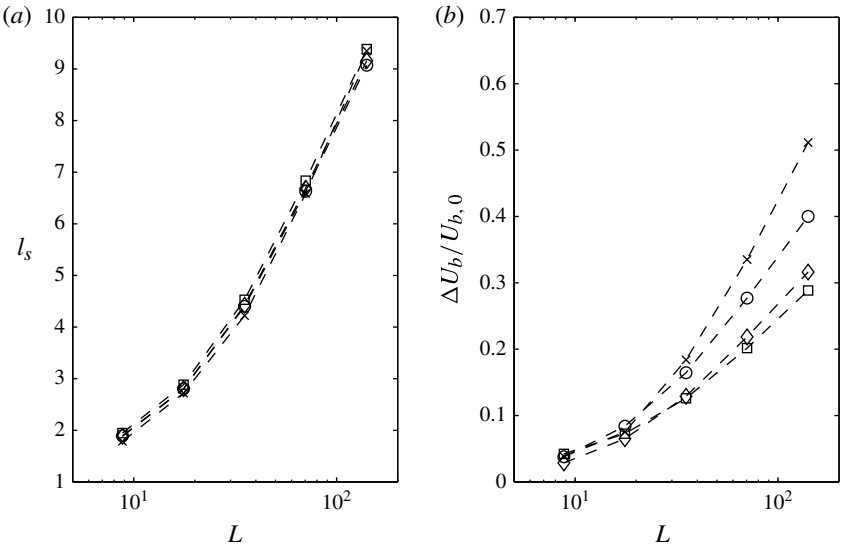

FIGURE 22. Model predictions of l_s and ΔU_b for different geometrical wavelengths, L, at different Reynolds numbers, Re_τ, with a solid fraction $\Phi = 0.5$: $\times$, model $Re_\tau = 180$; ●, model $Re_\tau = 10^3$; ◇, model $Re_\tau = 10^4$; □, model $Re_\tau = 10^5$.

or CPG is applied: while CFR leads to a reduction of the friction drag and is thus likely to be accompanied by relaminarization effects at the Reynolds numbers for which numerical parameter studies can be carried out, CPG leads to an increase of the flow rate. This difference between CFR and CPG, which is present for any type of skin friction drag variation, is visualized in figure 23(*a*,*b*). The comparison of the flow fields in figure 23(*b*,*c*) shows what is demonstrated by the statistics presented in the paper: the SHS model based on a homogeneously prescribed slip length leads to similar results as the present model with spanwise alternating boundary conditions.

The main advantage of the resolved boundary condition is the determination of the effective slip length, l_s, as a result of the flow over SHS instead of its *a priori* postulation. In the present paper, it is shown that the analytical solution for l_s in the Stokes flow regime (Philip 1972) also holds under turbulent flow conditions for small spanwise extends of the free-slip surface, i.e. $(1 - \Phi)L < 20$ (in wall units). In this case, the small wall-normal distance required to reach a homogeneous flow state in spanwise direction ensures that the effects of turbulent diffusion also remain small, and thus do not induce any significant differences. For larger values of L, l_s is found to be smaller in turbulent flows than under laminar flow conditions.

The CPG flow condition allows deriving a simple mathematical relationship between the resultant bulk mean velocity and different dynamical contributions, i.e. the effective slip length, l_s, and additional turbulent losses, ΔU_{loss}. The present analysis shows that the increase in the bulk mean velocity over SHS is mainly governed by l_s. The limited increase of l_s for larger L under turbulent flow conditions is shown to be related to two aspects. First, the turbulent diffusion decreases the effectiveness of the free-slip areas if the resulting spanwise inhomogeneities penetrate further from the wall. Second, the alternating free-slip and no-slip boundary condition causes a spanwise inhomogeneity which induces a secondary flow of Prandtl's second kind, characterized by steady streamwise roll cells. For large free-slip areas, the occurrence

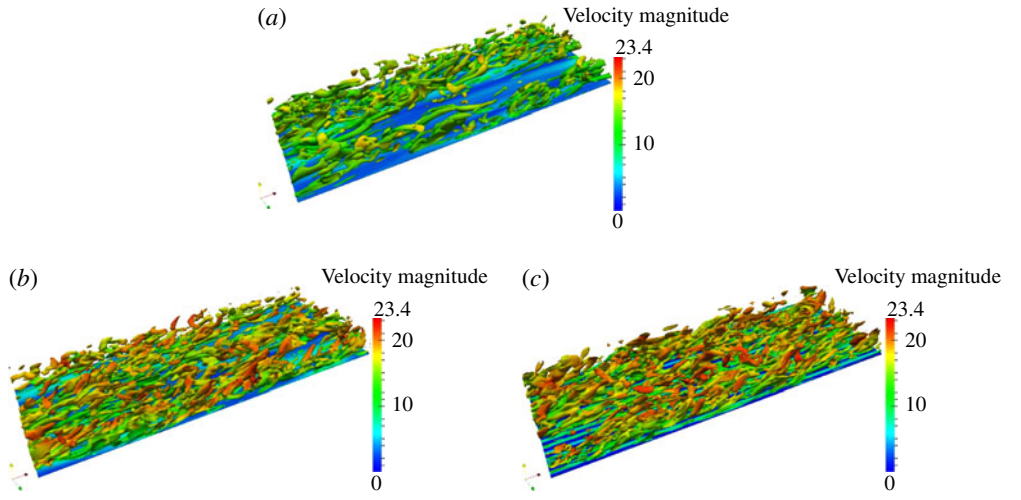

FIGURE 23. Isosurfaces of $\lambda_2 = -0.005$ (normalized by $u^*_{\tau,0}$) coloured by velocity magnitude: (*a*) CFR homogeneous slip $l_s = 3.566$; (*b*) CPG homogeneous slip $l_s = 3.566$; (*c*) CPG for $L = 35.2$ resulting in $l_s = 3.877$. The no-slip reference case for all simulations is set at $Re_\tau = 180$.

of tertiary vortices with opposed rotational direction is observed. The influence of the induced secondary motions on l_s is found to be significant only when tertiary vortices occur. They apparently limit the maximum achievable flow rate with SHS consisting of streamwise grooves with the solid fraction of $\Phi = 0.5$ under CPG to $\sim$1.5 times the flow rate in a channel with no-slip surfaces. Considering the fact that such wide cavities with a dimension in the order of the channel height are difficult to realize for turbulent flow conditions (see appendix A), the present results suggest that it is sufficient to consider the effect of turbulent mixing, i.e. the turbulent eddy viscosity, for an estimation of l_s and the corresponding flow rate increase.

The additional turbulent losses, ΔU_{loss}, increase with increasing L and reach an upper limit that is in agreement with results obtained for a prescribed partial slip in spanwise direction, l_s^z (Busse & Sandham 2012). An empirical correlation that links ΔU_{loss} to the geometrical properties of the surface structure with streamwise grooves is presented without any claim for generalization. Such a generalization is difficult since a clear definition of l_s^z, i.e. an effective slip length when no mean flow is present, cannot be given in a straightforward manner and, to the best of the authors' knowledge, does not exist in literature. The observed secondary and tertiary vortices also influence ΔU_{loss}. Interestingly, the tertiary vortices can induce a positive coherent contribution to the Reynolds shear stress and thus limit the turbulent losses.

Based on the results of the present study a simple modelling strategy for turbulent flows over SHS is established: for a spanwise width of the free-slip section of approximately $(1 - \Phi)L < 20$ the laminar prediction of l_s is combined with the prediction of ΔU_{loss} which yields good agreement with the DNS data. For larger values of L the effect of turbulent mixing is introduced by formulating a characteristic eddy viscosity based on the geometrical properties of the surface structure in combination with literature data for purely no-slip and free-slip boundaries. Although this model formulation is rather crude, it yields reasonable agreement with the present DNS data and can be used to estimate the effectiveness of SHS at larger Reynolds

numbers up to approximately $(1 - \Phi)L < 75$. Naturally, these model predictions are restricted to the validity of the underlying assumptions, especially the existence of a flat, stable and steady water–air interface.

Acknowledgements

The authors gratefully acknowledge support of project FR2823/2-1 of the German Research Foundation (DFG) and the Center of Smart Interfaces at TU Darmstadt. S.T. acknowledges the support from the Excellence Initiative of the German Federal and State Governments and the Graduate School of Computational Engineering at TU Darmstadt. Y.H. acknowledges the support from the Japan Society for the Promotion of Science (JSPS) Postdoctoral Fellowship for Research Abroad, and also the support of the Grant-in-Aid for Scientific Research (B) (No. 25289037) by the Ministry of Education, Culture, Sports, Science and Technology (MEXT).

Appendix. Realistic cavity width under turbulent flow conditions

In order to realize the boundary conditions of the present DNS in practice, it has to be guaranteed that the surface tension is strong enough to maintain the air–water interface under a background turbulent pressure fluctuation. In fully developed wall turbulence, the static pressure fluctuation p^*_{rms} can be scaled by

$$p^*_{rms} \sim O(\rho^* u^{*2}_\tau). \tag{A 1}$$

It should be noted that the above value also corresponds to the mean static pressure difference at different streamwise locations separated by a channel half-depth for internal flows.

Considering that the width of the cavity (free-slip region) cannot be larger than the period L of the SHS, the capillary pressure can be estimated as

$$p^*_c \sim O\left(\frac{\sigma^*}{L^*}\right). \tag{A 2}$$

Therefore, in order for the capillary pressure to overcome the background pressure fluctuation, the following condition has to be met:

$$O\left(\frac{\sigma^*}{L^*}\right) \gg O(\rho^* u^{*2}_\tau). \tag{A 3}$$

This can be also rewritten as

$$L \ll O\left(Ca^{-1}\right), \tag{A 4}$$

where the capillary number is defined as $Ca = \mu^* u^*_\tau / \sigma^*$.

Suppose we consider water under the standard condition as a working fluid, $\mu^* \approx 0.00089$ (Pa s) and $\sigma^* \approx 0.073$ (N m^{-1}). Taking a typical value of the friction velocity as $u^*_\tau = 0.5$ (m s^{-1}), the above equation indicates that $L \ll 160$. Note that the criteria is inversely proportional to u^*_τ, so that L generally has to be smaller with increasing the free stream (or bulk) velocity. It is therefore unlikely that the largest wavelengths of the streamwise grooves investigated in the present study can remain in the Cassie state.

Equation (A 4) can also be written as

$$Re_\tau \ll O\left(\frac{1}{L}\left(\frac{\rho^*\sigma^*\delta^*}{\mu^{*2}}\right)\right). \tag{A 5}$$

As shown in figure 15, the gain of a SHS saturates beyond $L^+ \approx 100$. If we aim to achieve $L^+ = 100$ for a channel half-height of $\delta^* = 0.1$ (m), the above equation indicates that $Re_\tau \ll O\left(10^5\right)$. It is also evident from (A 5) that this restriction on Re is mitigated when we increase the channel height and compromise L.

REFERENCES

BUSSE, A. & SANDHAM, N. D. 2012 Influence of an anisotropic slip-length boundary condition on turbulent channel flow. *Phys. Fluids* **24** (5), 055111.

CASSIE, A. B. D. & BAXTER, S. 1944 Wettability of porous surfaces. *Trans. Faraday Soc.* **40**, 546–551.

DANIELLO, R., WATERHOUSE, N. & ROTHSTEIN, J. 2009 Drag reduction in turbulent flows over superhydrophobic surfaces. *Phys. Fluids* **21** (8), 085103.

FROHNAPFEL, B., HASEGAWA, Y. & QUADRIO, M. 2012 Money versus time: evaluation of flow control in terms of energy consumption and convenience. *J. Fluid Mech.* **700**, 406–418.

FUKAGATA, K., IWAMOTO, K. & KASAGI, N. 2002 Contribution of Reynolds stress distribution to the skin friction in wall-bounded flows. *Phys. Fluids* **14** (11), L73.

FUKAGATA, K., KASAGI, N. & KOUMOUTSAKOS, P. 2006 A theoretical prediction of friction drag reduction in turbulent flow by superhydrophobic surfaces. *Phys. Fluids* **18** (5), 051703.

FUKAGATA, K., KOBAYASHI, M. & KASAGI, N. 2010 On the friction drag reduction effect by a control of large-scale turbulent structures. *J. Fluid Sci. Technol.* **5** (3), 574–584.

GAD-EL-HAK, M. 2007 *Flow Control: Passive, Active, and Reactive Flow Management*. Cambridge University Press.

GOLDSTEIN, D. B. & TUAN, T. -C. 1998 Secondary flow induced by riblets. *J. Fluid Mech.* **363**, 115–151.

HASEGAWA, Y., FROHNAPFEL, B. & KASAGI, N. 2011 Effects of spatially varying slip length on friction drag reduction in wall turbulence. *J. Phys.: Conf. Ser.* **318** (2), 022028.

HASEGAWA, Y. & KASAGI, N. 2007 Effects of interfacial velocity boundary condition on turbulent mass transfer at high Schmidt numbers. *Intl J. Heat Fluid Flow* **28** (6), 1192–1203.

KIM, J., MOIN, P. & MOSER, R. 1987 Turbulence statistics in fully developed channel flow at low Reynolds number. *J. Fluid Mech.* **177**, 133–166.

LAUGA, E. & STONE, H. A. 2003 Effective slip in pressure-driven Stokes flow. *J. Fluid Mech.* **489**, 55–77.

MARTELL, M. B., PEROT, J. B. & ROTHSTEIN, J. P. 2009 Direct numerical simulations of turbulent flows over superhydrophobic surfaces. *J. Fluid Mech.* **620**, 31–41.

MARTELL, M. B., ROTHSTEIN, J. P. & PEROT, J. B. 2010 An analysis of superhydrophobic turbulent drag reduction mechanisms using direct numerical simulation. *Phys. Fluids* **22** (6), 065102.

MARUSIC, I., JOSEPH, D. D. & MAHESH, K. 2007 Laminar and turbulent comparisons for channel flow and flow control. *J. Fluid Mech.* **570**, 467–477.

MAYNES, D., JEFFS, K., WOOLFORD, B. & WEBB, B. W. 2007 Laminar flow in a microchannel with hydrophobic surface patterned microribs oriented parallel to the flow direction. *Phys. Fluids* **19** (9), 093603.

MIN, T. & KIM, J. 2004 Effects of hydrophobic surface on skin-friction drag. *Phys. Fluids* **16** (7), L55.

NAVIER, C. 1823 Memoire sur les dois du mouvement des fluides. *Mem. Acad. Sci. Inst. Fr.* **6**, 389–440.

NIKURADSE, J. 1926 *Untersuchungen über die Geschwindigkeitsverteilung in turbulenten Strömungen*. vol. 281. VDI Forschungsheft.

OU, J., PEROT, B. & ROTHSTEIN, J. P. 2004 Laminar drag reduction in microchannels using ultrahydrophobic surfaces. *Phys. Fluids* **16** (12), 4635.

PHILIP, J. R. 1972 Flows satisfying mixed no-slip and no-shear conditions. *Z. Angew. Math. Phys.* **23** (3), 353–372.

PÖSCHL, TH. 1926 Zweiter internationaler kongreß für technische mechanik in Zürich. (12. bis 17. September 1926). *Naturwissenschaften* **14**, 1029–1032.

REYNOLDS, W. C. & HUSSAIN, A. K. M. F. 1972 The mechanics of an organized wave in turbulent shear flow. Part 3. Theoretical models and comparisons with experiments. *J. Fluid Mech.* **54** (02), 263–288.

ROTHSTEIN, J. P. 2010 Slip on superhydrophobic surfaces. *Annu. Rev. Fluid Mech.* **42** (1), 89–109.

SCHOPPA, W. & HUSSAIN, F. 1998 A large-scale control strategy for drag reduction in turbulent boundary layers. *Phys. Fluids* **10** (5), 1049–1051.

SPALART, P. R. & MCLEAN, J. D. 2011 Drag reduction: enticing turbulence, and then an industry. *Phil. Trans. R. Soc.* A **369** (1940), 1556–1569.

VAN DRIEST, E. R. 1956 On turbulent flow near a wall. *J. Aeronaut. Sci. (Inst. Aeronaut. Sci.)* **23** (11), 1007–1011.

WOOLFORD, B., MAYNES, D. & WEBB, B. W. 2008 Liquid flow through microchannels with grooved walls under wetting and superhydrophobic conditions. *Microfluid. Nanofluid.* **7** (1), 121–135.